Cleaner Materials 20 (2026) 100398

Contents lists available at ScienceDirect

Cleaner Materials

journal homepage: www.journals.elsevier.com/cleaner-materials

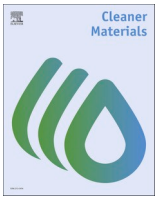

Valorisation of a waste derived from the decontamination of phosphogypsum leachate as a clay replacement in ceramics

F.J. Soto-Cruz [a], A. López-Delgado [b], I. Ramos-Lerate [a], J.P Bolívar [c], M.J. Gázquez [a], M. Romero [b,*]

[a] Department of Applied Physics, Marine Research Institute (INMAR), University of Cádiz, Campus de Excelencia Internacional del Mar (CEIMAR), Cádiz, Spain
[b] Eduardo Torroja Institute for Construction Sciences, IETcc-CSIC, Madrid, Spain
[c] Department of Applied Sciences, Research Centre On Natural Resources, Health and the Environment (RENSMA), University of Huelva, Huelva, Spain

ARTICLE INFO

Keywords:
Phosphogypsum leachate
Valorisation
Recycling
Traditional ceramics
Leaching test
Technological properties
Heavy metals immobilisation

ABSTRACT

This study presents the first valorisation of a waste generated from the cleaning process of phosphogypsum leachate (HApW) as a clay substitute in ceramics , contributing to the development of cleaner materials through industrial waste reuse. The waste is mainly composed of hydroxyapatite but contains non-negligible concentrations of heavy metals such as As, Zn, Cu, Ni, and V, and exhibits a ^{238}U activity concentration of approximately 750 $Bq{\cdot}kg^{-1}$. Ceramics were prepared with varying clay replacement by HApW (20, 40, 60, and 80 wt%). Two commercial ceramic clays with distinct chemical and mineralogical compositions (referred to as clay A and clay B) were used. The thermal behaviour, sintering responses and the resulting microstructural and mechanical properties were systematically evaluated to determine the suitability of HApW as a sustainable clay substitute. Ceramic compositions were further assessed for porosity, flexural strength, and environmental safety via leaching tests. Results indicate that high HApW compositions exhibit a mineralogy dominated by HApW derived phases, including substituted apatite ($Ca_5(Na,Mg)(PO_4)_3$) and complex calcium phosphate ($Ca_9MgNa(PO_4)_7$), formed through thermal decomposition. HApW induces intense sintering and high final shrinkage, and clay would act as a skeleton that moderates this process. The flexural strength of the ceramic compositions ranges from 7 to 47 MPa and decreases linearly with increasing HApW content; however, this behaviour depends not only on total porosity but also on pore size. Microstructural analysis showed that clay A led to mostly amorphous matrices, while clay B produced denser structures with integrated apatite and acicular mullite crystals, enhancing densification and mechanical performance. Environmental assessment showed that heavy metal release remains below regulatory limits and that the radiological impact is negligible (indicative dose < 0.1 $mSv{\cdot}year^{-1}$). Compositional evaluation against ISO 13006 ceramic tile requirements showed that formulations 50A and 60A meet the specifications for BIIa indoor floor tiles, whereas 70B and 80B comply with BIb requirements, identifying these compositions as the optimal ranges for practical application. These findings demonstrate the viability of HApW as a sustainable clay replacement in ceramic production within the framework of cleaner material development.

1. Introduction

In the context of the circular economy, the valorisation of waste plays an essential role in transforming waste into valuable resources, improving both the economic efficiency of companies and providing environmental benefits through reuse and recycling, using the approach of 'waste-to-resource innovation' (Leder et al., 2020; Ling et al., 2025).

From an environmental impact point of view, industrial waste generated and/or stored is as important as the leachates (the contaminated liquid produced by water percolating through solid waste) generated for them (. These effluents can contaminate soil, groundwater, and surface water with heavy metals, toxic chemicals, and other pollutants. This contamination can harm ecosystems, pollute drinking water, and pose risks to human health (Ayala and Fernández, 2020; Segundo et al., 2021).

A clear example of these leachates is the phosphogypsum leachate

* Corresponding author.
E-mail address: mromero@ietcc.csic.es (M. Romero).

https://doi.org/10.1016/j.clema.2026.100398
Received 16 January 2026; Received in revised form 23 April 2026; Accepted 24 April 2026
Available online 25 April 2026

(PGL), which is generated in phosphogypsum (PG) piles (Wu, 2024). Phosphogypsum is an inorganic waste (mainly composed of gypsum $CaSO_4{\cdot}2H_2O$) generated in the phosphoric acid production by using phosphate rock and sulphuric acid as raw materials (Bolívar et al., 1998; Tayibi et al., 2009). Currently, more than 300 million tonnes of phosphogypsum (PG) are produced annually, where only 14 % is recycled, 28 % is discharged into coastal waters, and the remaining 58 % is stored in stacks (Bilal et al., 2023). Thus, around 6–7 billion tonnes of phosphogypsum (PG) are estimated to be stored across the world to date (mainly EE.UU., Jordanian, Turkey, Tunisia, Spain, Morocco, China, Russia and Poland) (Chernysh et al., 2021). These stacks involve large open storage areas that are susceptible to leaching with the action of rainfall (Millán-Becerro et al., 2023; Millán-Becerro et al., 2019). Phosphogypsum leachate (PGL) is an environmental problem primarily due to its high content of pollutants, including heavy metals (lead, cadmium, arsenic, etc), radionuclides (U and Th decay family), and other toxic substances (F^-, SO_4^{2-} and Cl^-), which can contaminate soil, groundwater, and surface water (Wu, 2024). This contamination can lead to long-term ecological damage and pose health risks.

In Spain, the phosphogypsum stacks sited in Huelva (southwest of Spain) contain approximately 100 million tons of PG (after 45 years of phosphoric acid production). These stacks cover more than 1,000 ha in the marshlands of the Tinto River, less than one kilometre from the city. Previous studies have found that the contents in natural radioactivity of the PG are variable, with average values and ranges as follow: ^{226}Ra (650 $Bq{\cdot}kg^{-1}$, 400–1100 $Bq{\cdot}kg^{-1}$), ^{210}Pb = ^{210}Pb (500 $Bq{\cdot}kg^{-1}$, 300–600 $Bq{\cdot}kg^{-1}$), ^{238}U (120 $Bq{\cdot}kg^{-1}$, 30–300 $Bq{\cdot}kg^{-1}$), ^{230}Th (450 $Bq{\cdot}kg^{-1}$, 200–700 $Bq{\cdot}kg^{-1}$) (Bolívar et al., 1998; Mas et al., 2006). Additionally, with a pH = 1.5–3, the activity concentrations of PGL (collected in the perimeter channel, Fig. 1), are very high and variable, according to the solubility of the different radioelements. Thus, activity concentration for $^{238}U = {}^{234}U$ (200 $Bq{\cdot}L^{-1}$), ^{230}Th (0.8 $Bq{\cdot}L^{-1}$), ^{226}Ra (2 $Bq{\cdot}L^{-1}$), $^{210}Pb = {}^{210}Po$ (20 $Bq{\cdot}L^{-1}$) were measured (Gázquez et al., 2014; Guerrero et al., 2021). In relation to the metals and metalloids, concentrations of total phosphorus (10–32 $g{\cdot}L^{-1}$), fluorides (1.5–2 $g{\cdot}L^{-1}$), sulphates (4–5 $g{\cdot}L^{-1}$), chlorine (4.5–5.5 $mg{\cdot}L^{-1}$), and metals such as K (250–300 $mg{\cdot}L^{-1}$), Mg (600–700 $mg{\cdot}L^{-1}$), Ca (1600 $mg{\cdot}L^{-1}$), Na (3.5–4.5 $g{\cdot}L^{-1}$), As (25–50 $mg{\cdot}L^{-1}$), Zn (65–70 $mg{\cdot}L^{-1}$), Cr (20 $mg{\cdot}L^{-1}$), Cd (8 $mg{\cdot}L^{-1}$), Mg (700–900 $mg{\cdot}L^{-1}$) and Br (100 $mg{\cdot}L^{-1}$) were found (Soto-Cruz et al., 2024, 2025).

To mitigate the environmental impact of the PGL, Soto-Cruz et al. (Soto-Cruz et al., 2024) developed a treatment for the decontamination of PGL by adding $CaCO_3$ and $Ca(OH)_2$ in two sequential separate steps. As a result of this treatment, two solid wastes (one from each step) and a non-polluted liquid effluent were obtained. The first solid consisted mainly of calcium fluoride (37–55 wt% CaF_2), whereas the second solid, composed predominantly of hydroxyapatite (75–80 wt% $Ca_5(PO_4)_3OH$), is the waste investigated in the present study. For clarity, this second waste will hereafter be referred to as HApW. HApW contains high concentrations of phosphorous and calcium (in hydroxyapatite form) and potential hazardous substances such as heavy metals (Pb, Cr, As, etc) and natural radionuclides (mainly ^{238}U and ^{234}U).

Hydroxyapatite (HAp) is regarded as an environmentally friendly adsorbent due to its non-toxic nature and low solubility in water (Feng et al., 2010; Lin et al., 2023; Peng et al., 2023). Several studies have demonstrated that HAp obtained by hydrothermal processing of marble sludge and limestone sludge its effectiveness in removing Cu^{2+} and Pb^{2+} (Lin et al., 2023; Peng et al., 2023; Takei et al., 2013) from wastewater. Similarly, HAp obtained from the valorisation of calcium sulphite ($CaSO_3$) waste, was studied as good heavy metal adsorption material, particularly for removing Cs^+ and Cd^{2+} from aqueous solutions, offering a heavy metal pollution mitigation (Takei et al., 2013).

Similar wastes to HApW but obtained from other processes, were used in the manufacture of construction materials. In this sense, the sludge generated in the mining activity related to natural phosphate beneficiation (usually called phosphate sludge with concentration of 14 % P_2O_5 and 34 % of CaO) was mixed with natural clay (up to 30 %). This study demonstrated that phosphate sludge mixture with 5 % of clay and processed under specific thermal conditions (900–1000 °C), can be transformed into ceramic materials with enhanced physical properties (water absorption, density, and compressive strength) (Loutou et al., 2017). Bih et al. explored the use of hydroxyapatite (from bone ash), in clay bricks. The study found that adding 5 %, 10 %, and 15 % bone ash resulted in compressive strengths of ~ 41.6 MPa, ~ 49.3 MPa, and 46.1 MPa, respectively, compared to the control clay bricks at 20 MPa. Additionally, bricks containing bone ash tend to have lower water absorption due to decreased porosity, improving their performance (Bih et al., 2022). Moreover, a study by Avelino et al. demonstrated that the addition of natural HAp led to a reduction in water absorption and apparent porosity, and a significant increase in the linear shrinkage and mechanical resistance of ceramic pieces, achieving up to 25 % greater strength compared to formulations without HAp (Avelino et al., 2023).

Compared with other calcium-phosphate wastes previously studied for use in ceramics, the characteristics of HApW differ substantially.

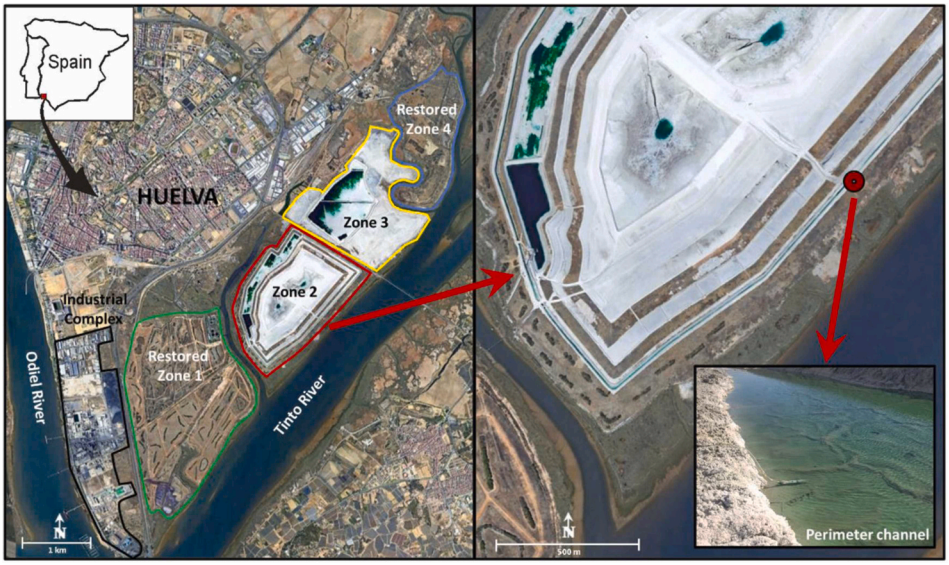

Fig. 1. Aerial view of the phosphogypsum stacks of Huelva and the location of the PGL collection channel. The image shows the large-scale phosphogypsum disposal area and the drainage system from which the phosphogypsum leachate (PGL) used in this study is collected.

Phosphogypsum mainly consists of $CaSO_4{\cdot}2H_2O$ and has a very low phosphate content. It also does not exhibit the thermal reactivity associated with calcium phosphates. Phosphate sludge usually contains fluorapatite mixed with silicates and only develops moderate melt formation during firing. On the other hand, bone-ash-derived hydroxyapatite is highly crystalline and almost entirely free of environmentally significant impurities, resulting in a comparatively weak effect on sintering behaviour. Therefore, these residues differ significantly from the HApW waste in both origin and thermal response.

Nevertheless, while several authors have explored the reuse of hydroxyapatite-containing waste materials such as bone ash, marble sludge, calcium sulphite residues and phosphate sludge in ceramics or construction materials, the residue investigated here (named HApW) is fundamentally different. HApW is derived from the second stage of a particular $CaCO_3/Ca(OH)_2$ decontamination process used for treating phosphogypsum leachates. Consequently, it contains a combination of hydroxyapatite, amorphous calcium phosphate, heavy metals, and U-series radionuclides. To our knowledge, no previous study has evaluated the valorisation of this type of waste as a clay substitute.

The behaviour of clay-based ceramics during firing is largely governed by the mineralogical transformations of kaolinite, illite, and muscovite, as well as the formation of liquid phases that control densification (Kingery et al., 1976; Kalendova et al., 2024). Additionally, incorporating waste materials into ceramic bodies has been extensively studied as a valorisation strategy, with the final properties strongly dependent on fluxing oxides and interactions with the aluminosilicate matrix (Zanelli et al., 2021; Romero et al., 2021; Martín et al., 2013).

Considering the previous mentioned, the objective of this study is to analyse the incorporation of waste from the second step of decontamination process for PGL as clay substitute in the manufacture of commercial ceramics, and to evaluate its impact on sintering behaviour, mineralogical evolution, microstructure, mechanical performance, and the environmental and radiological safety of end products. These combined aspects (raw material origin, compositional uniqueness, environmental relevance and functional behaviour) represent the main novelty of the present study within the framework of cleaner materials development, where industrial by-products are reintroduced into high-value applications to reduce waste generation and resource consumption. In addition, given that the optimal formulations identified in this study incorporate 50–80 wt% HApW, this approach has realistic potential to valorise several tonnes of this residue annually in industrial ceramic production, thereby enhancing technological and environmental viability.

2. Materials and methods

2.1. Raw materials

The raw materials used in this study were an industrial waste and two commercial clays. The waste was a material rich in hydroxyapatite (HApW), obtained from PGL collected at the phosphogypsum stockpiles located in Huelva (south-west Spain). This waste was extensively characterised in a previous study (Soto-Cruz et al., 2024). In addition, two different commercial clays, clay A and clay B, were used as primary sources of silica and alumina. Both clays are widely used in industrial ceramic tile formulations. They were selected because they are representative of two typical raw materials with distinct mineralogical compositions and fluxing behaviours. Using both clays enables the assessment of the behaviour of HApW under two representative industrial ceramic matrices with different sintering reactivities. Clay A contains the main oxides SiO_2 (59.79 %) and Al_2O_3 (33.19 %), supplemented by fluxing oxides such as Fe_2O_3 (2.29 %) and K_2O (2.29 %), and other minor alkaline earth oxides. Mineralogically, this clay is primarily composed of kaolinite ($Al_2Si_2O_5(OH)_4$), with smaller amounts of quartz (SiO_2) and muscovite ($KAl_2(AlSi_3O_{10})(OH)_2$). Clay B, on the other hand, has a composition of SiO_2 (54.53 %) and Al_2O_3 (34.89 %), with a higher content of fluxing oxides, particularly Fe_2O_3 (5.22 %), K_2O (2.88 %), and TiO_2 (1.01 %). The mineralogical composition of clay B is dominated by muscovite, with quartz and kaolinite in smaller proportions. This suggests a greater potential for liquid-phase formation at lower temperatures owing to the contribution of fluxes associated with muscovite.

2.2. Sample preparation

The test specimen preparation process began with the pre-treatment of raw materials to break soft agglomerates and ensure homogeneous mixing of the raw materials. The HApW was ground in a Retsch 100 PM ball mill and sieved to achieve a particle size of less than 200 μm. Subsequently, it was fractionated to obtain representative samples. Binary compositions were then defined by mixing HApW with one of the clays. The nomenclature of the samples reflects the percentage of clay in the mixture (a number, e.g., 80) and the clay code: A for clay A and B for clay B (for example, 80A corresponds to the mixture 20 wt% HApW plus 80 wt% clay A). These mixtures were homogenised in a TÚRBULA planetary mixer with alumina balls to ensure uniform distribution of the components. Finally, the powders were formed by uniaxial pressing at 40 MPa under wet conditions (using 5 % water to improve agglomeration and compaction). Two test piece geometries were prepared: 2 cm diameter discs from 1.5 g of mixture and parallelepiped test pieces 5.3 cm long and 1.6 cm wide from 6 g of mixture. All test pieces were kept in an oven at 110 °C for a minimum of 24 h for drying before firing. Finally, the firing schedule consisted of several controlled heating ramps adjusted to reach the target temperature within approximately 45 min. The maximum temperature was held for 30 min, after which the specimens were cooled inside the furnace under a controlled cooling ramp designed to reach room temperature in approximately 25 min.

2.3. Analytical methods

Chemical and quantitative analysis of the HApW was determined by X-ray fluorescence (XRF). The raw materials were prepared by grinding in a Retsch 100 PM ball mill and subsequent sieving to a particle size of less than 63 μm. The samples were then subjected to elemental analysis using a Bruker S8 Tiger X-ray fluorescence (XRF) spectrometer. The analytical procedure followed standard XRF guidelines for ceramic and mineral raw materials (ISO 12677:2011 standard “Chemical analysis of refractory products by X-ray fluorescence (XRF) – Fused cast-bead method”).

The crystalline structure of the raw materials and fired ceramic was analysed using X-ray diffraction (XRD). To this end, the samples were ground and sieved in advance to achieve a particle size of less than 63 μm. Analysis was carried out using a Bruker D8 Advance diffractometer with CuKα radiation, an intensity of 30 mA and a voltage of 50 kV. The scan was performed within an angular range of $3^\circ \leq 2\theta \leq 60^\circ$ at a speed of 0.5° min. Each crystalline phase in the diffractograms was identified using Bruker DIFFRAC.EVA V4.2.1 software. XRD analysis and phase identification were performed according to the general recommendations of EN UNE-EN 13925–2:2004 standard “Non-destructive testing − X-ray diffraction from polycrystalline and amorphous materials − Part 2: Procedures”.

The thermal stability of HApW was analysed using differential thermal and thermogravimetric analysis (DTA/TG) with TA Instruments SDT Q600 equipment. For this study, a 5 mg sample was heated from room temperature to 1300 °C at a rate of 50 $^\circ C{\cdot}min^{-1}$ under a constant airflow. The sample was placed in an alumina crucible, with calcined Al_2O_3 used as the reference material. To ensure homogeneity, the HApW samples were pre-ground and sieved to a particle size of less than 63 μm.

The dimensional changes in the samples during the firing process were evaluated using heating microscopy (HM) in a Hesse Instruments model HR18 device. This system comprises a chamber connected to a tubular furnace, as well as image analysis software that enables

continuous monitoring of dimensional variations. The test was carried out in an oxidising atmosphere (air) at a constant heating rate of 10 °C·min^{-1}, with the samples supported by alumina. This characterisation was performed on both the individual raw materials and all the raw ceramic compositions. To this end, powder samples were sieved to a particle size of less than 63 μm and then shaped into prisms.

The total porosity and average pore diameter of the fired ceramic samples were determined using X-ray computed tomography (CT) on a Nikon CT-SCAN-XT H-160 device. This was equipped with a tungsten lens, operated at 82 kV and 51 mA, and took 1000 projections over an exposure time of 1000 ms. No prior preparation of the samples was required for analysis.

The flexural strength of the sintered ceramic specimens was determined by means of three-point flexural tests on parallelepiped specimens, in accordance with the requirements of the UNE-EN 843–1 standard "'Advanced technical ceramics, monolithic ceramics". Mechanical properties at room temperature". Part 1: Determination of Flexural Strength"). The tests were performed using a Servosis ME-402/01 hydraulic press controlled by PCD-2 K software. The distance between the press's rollers was set to 3 cm, and the load speed was adjusted so that the specimen would break within 5–15 s.

The microstructure of the ceramics was characterised using a Field Emission Scanning Electron Microscope (FESEM) operating at an accelerating voltage of 20 kV. SEM observations were carried out on freshly fractured samples coated with a carbon layer using a Quorum Technologies Q150T sputter. Semiquantitative analysis of the different phases was performed using Energy Dispersive X-ray Spectroscopy (EDS) with a Link eXL detector fitted with a beryllium (Be) window. Digital X-ray mapping was used to thoroughly investigate the spatial distribution of the various elements across the material.

2.4. Leaching hazard assessment and radioactivity analysis

The leaching of pollutants in the specimens was assessed using a modified version of the UNE-EN 12457–2:2003 "Characterisation of waste Leaching Compliance test for leaching of granular waste materials and sludges". Monolithic specimens were employed instead of particles < 4 mm to better reflect the actual release mechanisms of pollutants under service conditions. Demineralised water was used as the extraction fluid, maintaining a liquid-to-solid ratio of 10 L·kg^{-1} (± 2 %) and a leaching duration of (24 ± 0.5) h. Monolithic specimens were submerged in demineralised water for 24 h with agitation.

Following this period, the leachate was collected and analysed using: (1) Inductively Coupled Plasma Optical Emission Spectrometry (ICP-OES, SPECTRO model FMD46) at the Central Research Services (University of Cadiz). ICP-OES quantification followed the general analytical framework of ISO 17294–2:2013 "Water quality – Application of inductively coupled plasma mass spectrometry (ICP-MS) – Part 2: Determination of selected elements including uranium isotopes (ISO)"; (2) Alpha and gamma spectrometry were used for the radioactivity analysis. For alpha-particle spectrometry an EG&ORTEC system with an integrated Octete PC PLUS was used. The samples were firstly subjected to the sequential separation method by using TRU resin (Gázquez et al., 2022). Afterwards, U isotopes were electrodeposited onto stainless steel discs. Finally, the Maestro software was used for data analysis and acquisition. For gamma spectrometry, an extended range (XtRa) high-purity germanium detector (model GX3519, Canberra) was used in the energy range from 0 to 3 MeV. The relative efficiency was 38.4 % at 1332 keV (60Co) in relation to a 3″ × 3″ NaI (Tl) detector, a full width at half maximum (FWHM) of 1.74 keV and 0.88 keV at 1332 keV (60Co) and 122 keV (57Co), respectively, and a peak-to-Compton ratio of 67.5:1. Gamma spectrometry measurements followed the guidelines of UNE-EN ISO 18589–3:2024 "Measurement of radioactivity in the environment – Soil – Part 3: Test method of gamma-emitting radionuclides using gamma-ray spectrometry". All the tests were conducted in triplicate, with blanks included for every ten samples to ensure data reliability. Gamma spectroscopy was also used to characterise the ceramics compositions and index *I* was calculated.

3. Results and discussion

3.1. Raw material characterisation

3.1.1. Chemical characterisation of HApW

The chemical composition of the HApW, as determined by XRF, is presented in Table 1. The analysis reveals that the primary constituents are calcium oxide and phosphorus pentoxide, with concentrations of 46.77 wt% and 27.99 wt%, respectively. These values support that the waste material is predominantly a calcium phosphate-based compound, consistent with the expected composition of hydroxyapatite. The calculated weight ratio of CaO/P_2O_5 for this waste material is approximately 1.67. This ratio deviates from the theoretical value of 1.317 for stoichiometric hydroxyapatite ($Ca_{10}(PO_4)_6(OH)_2$), indicating potential non-stoichiometry or the presence of other calcium- or phosphate-containing phases within the waste.

It also contains Na_2O and MgO as minor oxides, which could act as sintering agents as they are low-temperature fluxes. It also contains impurities such as Cl and SO_3. In addition to the main components, the analysis identifies several minor elements present at concentrations above 1 wt%. These include magnesium and sodium oxides, sulphur trioxide, and chlorine. A significant loss on ignition (LOI) of 13.58 wt% is recorded for this sample. This high value suggests the presence of a substantial number of volatile components beyond the structural water content expected in pure hydroxyapatite. These components may include adsorbed water, structurally bound water within an amorphous phase, carbonates, and residual organic matter.

Trace amounts (below 0.1 wt%) of other oxides and elements are also detected. Although present in small quantities, these impurities can potentially influence ceramic processing and the final material properties (Wu et al., 2023). Notably, the presence of heavy metals such as arsenic, copper and nickel necessitate careful consideration of its potential environmental implications (Wu, 2024; Yan et al., 2024).

According to the radioactive analysis reported in our previous work (Soto-Cruz et al., 2024), the activity concentrations of the radionuclides were as follows: ^{238}U (750 ± 20 Bq·kg^{-1}), ^{210}Po (58 ± 5 Bq·kg^{-1}), ^{232}Th (< 0.4 Bq·kg^{-1}), ^{210}Pb (< 100 Bq·kg^{-1}), ^{226}Ra (< 20 Bq·kg^{-1}), ^{228}Ra (< 40 Bq·kg^{-1}), ^{228}Th (< 15 Bq·kg^{-1}), and ^{40}K (44 ± 12 Bq·kg^{-1}). In this case, the radionuclides in the waste are not in secular equilibrium. Therefore, this aspect must be considered and will be further discussed in Section 3.6 (Environmental Impact).

For comparison purposes, the activity concentrations of the radionuclides commonly evaluated in building materials (^{232}Th, ^{226}Ra, and

Table 1
Chemical composition of the HApW (wt.%) as determined by XRF.

	HApW (wt.%)
CaO	46.77
P_2O_5	27.99
MgO	3.19
SO_3	2.51
Na_2O	2.38
Cl	2.31
SiO_2	0.54
Al_2O_3	0.27
K_2O	0.13
ZnO	0.09
As_2O_3	0.06
V_2O_5	0.03
MnO	0.03
Fe_2O_3	0.03
CuO	0.02
NiO	0.01
LOI	13.58

^{40}K) are below the worldwide average values reported for such materials (50 Bq·kg^{-1} for ^{232}Th, 50 Bq·kg^{-1} for ^{226}Ra and 500 Bq·kg^{-1} for ^{40}K) (UNSCEAR, 1993 (Annex A)). In contrast, the radionuclide with the highest activity concentration in our sample is ^{238}U. Elevated concentrations of this radionuclide have been reported in clays and shales. For instance, clays from Malaysia (Abu Hanifah et al., 2023) have been reported to reach up to 1300 Bq·kg^{-1} of ^{238}U, while shales from Egypt (Ibrahim, 2024) and Morocco (Galindo et al., 2007) show values of up to 9000 and 500 Bq·kg^{-1} of ^{238}U, respectively. This variability in uranium activity concentrations in clay-based materials has also been highlighted in recent studies, which emphasize the strong influence of geological origin and mineralogical composition on natural radioactivity levels (Vasić et al, 2025).

3.1.2. Mineralogical analysis of HApW

The diffraction pattern of the HApW is shown in Fig. 2. The presence of crystalline phases is revealed by the occurrence of distinct peaks, and a comparison with the reference pattern for hydroxyapatite (HAp) (PDF 03–0747) shows a good match between the observed peaks and the characteristic diffractions of $Ca_{10}(PO_4)_6(OH)_2$. The presence of these characteristic peaks confirms that hydroxyapatite is the primary crystalline phase. However, the diffractogram also exhibits a significant increase in the background intensity, particularly at lower 2θ angles. This broad hump indicates the presence of a substantial amount of amorphous or poorly crystalline material in the sample.

The crystalline peaks of hydroxyapatite appear relatively broad and of moderate intensity, suggesting a nanocrystalline nature or the presence of lattice strain within the crystalline domains (Cao et al., 2007). The absence of sharp, distinct peaks corresponding to other crystalline phases suggests that the impurities identified in the chemical analysis (e.g., oxides of magnesium, sodium, and sulphur) are either present in amorphous forms or their concentration is below the detection limit of the XRD technique.

The strong amorphous background is consistent with the high loss on ignition (LOI) observed in the chemical analysis, suggesting that a significant portion of the volatile components may be associated with a non-crystalline fraction. This amorphous phase could be also attributed to amorphous calcium phosphate (ACP) or other poorly ordered calcium phosphate precursors. ACP is a well-known precursor in the formation of hydroxyapatite, being a metastable phase that tends to transform into the thermodynamically more stable crystalline hydroxyapatite (Nakashima et al., 2024).

3.2. DTA/TG analysis of HApW

Fig. 3 depicts the DTA/TG analysis of the HApW. The TG curve shows a total mass loss of approximately 16.75 % across the analysed temperature range, correlating with the high LOI value from the chemical analysis and further supporting the presence of a substantial amorphous phase with bound water and/or other volatile species, consistent with the XRD findings of a strong amorphous background.

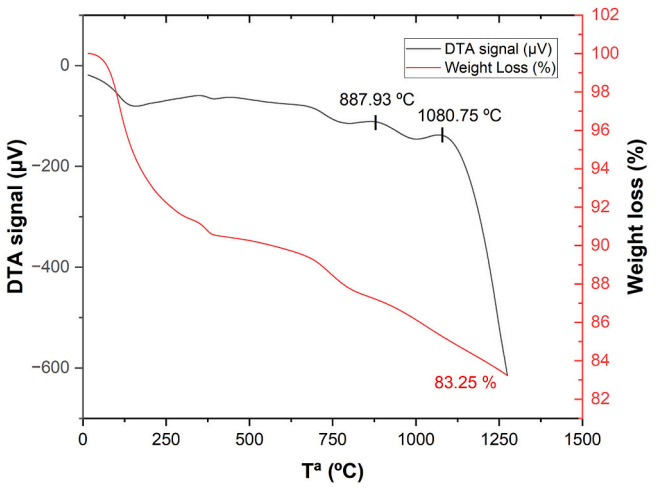

Fig. 3. DTA/TG analysis of the HApW showing progressive mass loss and the main thermal events associated with ACP crystallisation and HAp dehydroxylation.

This mass loss is associated with several thermal events observed in the DTA curve. A broad and shallow endothermic peak is observed below 200 °C, which is primarily attributed to the release of adsorbed water from the surface of the waste material and the initial dehydration of the amorphous phase. The mass loss in the intermediate temperature range (200–800 °C) likely corresponds to the continued dehydration of the amorphous phase and the removal of any remaining volatile components without significant sharp thermal events in the DTA curve. A distinct exothermic peak is evident at approximately 887 °C, which is likely due to the crystallization of ACP into a more thermodynamically stable crystalline phase (Uskoković et al., 2018) or the oxidation of residual organic impurities in the sample. Finally, a significant and sharp decrease in the heat flow begins at approximately 1080 °C, which is primarily attributed to the dehydroxylation of the crystalline HAp structure (Raynaud et al., 2002), leading to the formation of anhydrous calcium phosphate phases such as tricalcium phosphate (TCP) and possibly calcium oxide (CaO). The subsequent endothermic drop in the DTA signal suggests the onset of melting or the formation of a liquid phase within the system as decomposition progresses.

3.2.1. Heating microscopy analysis of the raw materials

Fig. 4 shows the heating microscopy curve for the HApW. From room temperature to approximately 450 °C, the material exhibits remarkable

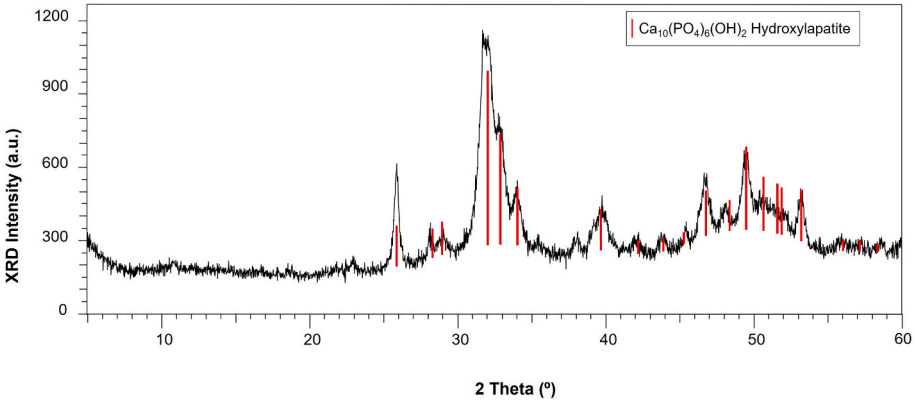

Fig. 2. Diffraction pattern of the HApW showing broad amorphous background and the main crystalline peaks characteristic of hydroxyapatite.

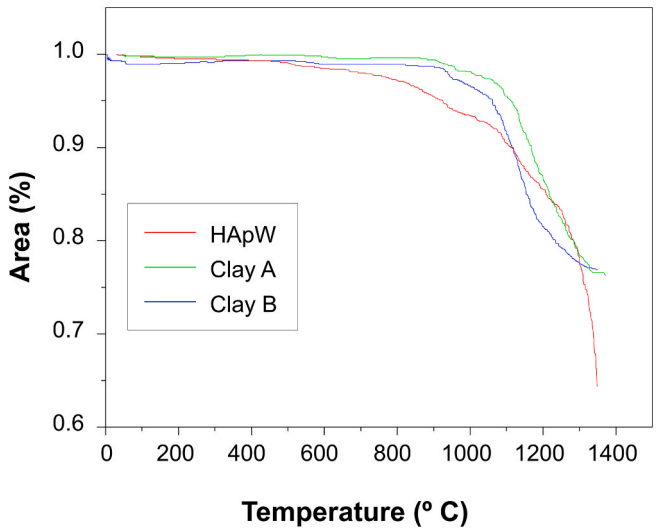

Fig. 4. Heating microscopy curves for the HApW, clay A, and clay B, highlighting their different shrinkage onsets and final densification behaviours.

dimensional stability with no observable shrinkage. This initial plateau indicates that the material retains its original geometry during the early stages of heating, suggesting the absence of significant low-temperature densification processes or phase transformations that induce volumetric changes. From 450 °C to approximately 900 °C, a slight and gradual contraction is observed, resulting in a reduction of approximately 1.5 % in the sample area. This moderate initial shrinkage could be due to the continued release of residual adsorbed water, initial densification processes associated with the amorphous phase, and initial particle rearrangement. Beyond 900 °C, a distinct and rapid contraction phase begins, leading to a total area reduction of around 36 %. This sharp decrease in the specimen area indicates the onset of active sintering and densification. This significant shrinkage is consistent with the thermal events observed in Fig. 3, particularly the strong endothermic event that initiates around 1080 °C. This endothermic process is linked to the dehydroxylation of crystalline HAp and the decomposition of the amorphous calcium phosphate. This, in turn, facilitates the formation of more mobile species or even a liquid phase. The presence of such a liquid phase greatly increases mass transport, promoting highly efficient and rapid densification via liquid-phase sintering (Indurkar et al., 2021). Above 1320 °C, the curve decreases extremely sharply, indicating the extensive formation of a low-viscosity liquid phase, which could result in the sample losing its structural integrity completely.

The sintering behaviour of HApW highlights the necessity of incorporating additional raw materials to produce stable and durable ceramic products. To this end, two different clay materials (clay A and clay B) were selected, and their thermal behaviour was also investigated using heating microscopy (Fig. 4).

Clay B exhibits a more gradual and extended shrinkage profile than the HApW. Practically no shrinkage is noticeable from room temperature to approximately 900 °C. The major sintering phase occurs between 950 °C and 1200 °C, showing a steady reduction in area and indicating efficient densification without an abrupt deformation. Clay A also shows almost no shrinkage from room temperature to approximately 900 °C. From 900 °C onwards, clay A begins its main contraction phase, although at a slightly slower initial rate than clay B. The densification process is most significant between 1050 °C and 1300 °C. Despite their differing initial contraction rates, both clay B and clay A achieve a similar final level of densification within the studied temperature range, with an overall area contraction of approximately 23 % by 1370 °C.

Fig. 5 shows the heating microscopy curves for the formulations composed of the HApW waste and clay A or B. It is important to note that the behaviour observed in Fig. 5 does not arise solely from the HApW fraction. Both clays undergo their own mineralogical transformations during heating, including the dehydroxylation and structural collapse of kaolinite and muscovite at intermediate temperatures. These transformations also contribute to dimensional changes. Therefore, the sintering response of the mixtures results from the combined thermal evolution of the raw clays and the HApW. The curves show the role of HApW as a flux that modifies the clay sintering. Concerning compositions formulated with the clay B (Fig. 5b), in the initial temperature region, from room temperature to approximately 900 °C, clay-rich compositions (80B and 60B) exhibit remarkable dimensional stability, reflecting the intrinsic refractory behaviour of clay minerals at low temperatures. Conversely, the formulations with a high HApW content (40B and 20B) show a slight but noticeable decrease in the area above 500 °C. This behaviour is attributed to the gradual release of structurally bound water (Fig. 3) and the initial densification of the amorphous hydroxyapatite phase (Bulina et al., 2021). The onset of sintering, considered the point at which the curves clearly begin to descend, occurs within the 950–1050 °C range. Notably, mixtures with a higher proportion of HApW begin to shrink at slightly lower temperatures (approx. 950–1000 °C) than clay-rich mixtures (approx. 1000–1050 °C). This advance in the onset of sintering confirms the role of HApW in reducing the firing temperature and facilitating earlier intergranular bonding. The main densification stage occurs between 1100 and 1350 °C and shows the greatest reduction in area for all compositions. The acceleration of shrinkage from 1150 °C indicates that liquid-phase sintering is the main densification mechanism in this temperature range. The formation of a low-viscosity liquid phase resulting from the decomposition of HAp and its reaction with clay oxides (CaO, Na_2O, etc.) promotes

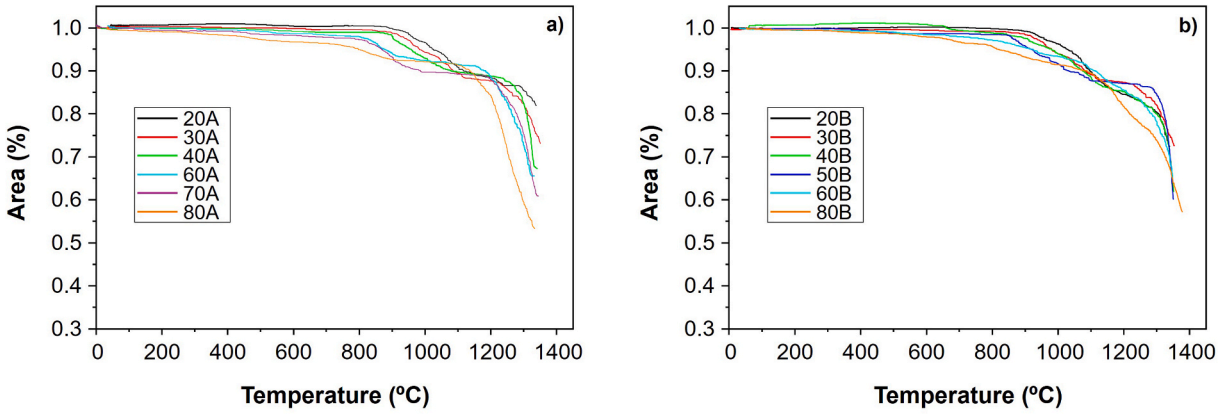

Fig. 5. Heating microscopy curves for the formulations composed of hydroxyapatite residue (HApW) and a) Clay A, and b) Clay B, showing how increasing the HApW content accelerates sintering and modifies the densification profile.

mass transport across grain boundaries, thereby accelerating shrinkage. The balance between the densifying behaviour of HApW and the refractory stability of clay is crucial for the viability of these formulations. While HApW induces intense sintering and high final shrinkage, clay acts as a skeleton that moderates this process. The composition with the highest clay content (80B) exhibits slightly higher stability up to approximately 1100 °C, acting as an initial retardant and providing a more controlled densification profile.

Finally, all the mixtures exhibit a sharp decrease in area at temperatures above 1350 °C, resulting in final area values ranging from 0.6 to 0.7. This behaviour indicates widespread overcooking. At this stage, the porous structure collapses owing to densification progressing to such a degree, which could be associated with glass softening and the material becoming viscous. Therefore, controlling the firing temperature is critical, and including excessive HApW in the formulation reduces the practical sintering window, increasing the risk of deformation or failure of the final product.

The heating microscopy curves of the HApW mixtures with clay A (Fig. 5a) show a sintering behaviour similar to that observed in the HApW-clay B system. In both families of compositions, HApW acts as a densifying agent that significantly influences the sintering process. The addition of HApW causes the mixtures to contract slightly at intermediate temperatures (approx. 500 °C) when the HApW content is high. The main sintering, characterised by a significant reduction in area, that begins in the 950–1050 °C range. The proportion of HApW in the formulation modulates the starting temperature and intensity of sintering, enabling densification at lower temperatures.

Although both systems exhibit similar overall behaviour, critical differences in their performance at high temperatures impact their processing viability. The main distinction lies in their high-temperature stability and sintering window. While mixtures with clay B demonstrate a greater ability to maintain their structural integrity, those with clay A, particularly those with a high HApW content, exhibit a more abrupt and severe collapse. This behaviour can be explained by the different roles played by the aluminosilicate matrices during high-temperature sintering. Clay A, with a higher SiO_2/Al_2O_3 ratio and lower content of fluxing oxides, tends to generate a more viscous liquid phase, which limits mass transport and increases the likelihood of pore retention and structural collapse when HApW content is high. In contrast, clay B contains higher levels of Fe_2O_3 and K_2O, which promote the formation of a more fluid liquid phase, enabling earlier densification and better dimensional stability. Consequently, the HApW-clay B system appears to offer a broader processing window and enhanced dimensional stability control compared with the HApW-clay A system. Clay B contains a high concentration of active fluxes (Fe_2O_3 at 5.22 % and K_2O at 2.88 %), which reduces the viscosity of the liquid phase to accelerate ion diffusion. This low final viscosity enables optimal sintering.

The firing temperatures for each composition series were selected based on the results of the heating microscopy analysis, to achieve effective densification while avoiding overfiring or collapse. For mixtures containing clay B, a temperature of 1150 °C was chosen because this is the point at which significant densification occurs without deformation, as indicated by the curves. Conversely, mixtures with clay A exhibited greater initial stability at intermediate temperatures and required additional thermal energy to initiate and complete the densification process. Therefore, a higher firing temperature of 1250 °C was selected for these samples. The firing temperatures were selected based on the heating microscopy results: clay B, which contains higher amounts of fluxing oxides, reached effective densification at 1150 °C, whereas clay A, characterised by a higher SiO_2/Al_2O_3 ratio and lower flux content, required 1250 °C to achieve comparable densification without deformation. The expected sintering mechanisms therefore differ between both systems, with clay B dominated by low-viscosity liquid-phase sintering and clay A by higher-viscosity melt formation and slower densification. Both firing temperatures fall within standard industrial ranges: flux-rich ceramic bodies are typically fired at 1100–1150 °C, while more refractory kaolinitic or porcelain-type bodies commonly require higher firing temperature (up to 1250 °C). Therefore, the selected temperatures are fully compatible with current kiln technologies and energy practices.

3.3. Mineralogical characterisation of the new materials

Fig. 6 shows the XRD results for the clay A and clay B mixtures fired at 1250 and 1150 °C, respectively. Compositions with a high HApW content (e.g. 20A and 30A) show a mineralogy dominated by phases derived directly from the HApW. The XRD patterns indicate a kinetic equilibrium of the calcium phosphate phases. The presence of both substituted apatite ($Ca_5(Na,Mg)(PO_4)_3$; PDF 89–6444) and a complex calcium phosphate ($Ca_9MgNa(PO_4)_7$; PDF 45–0136) is a direct result of the thermal decomposition of the initial HAp in the presence of impurities. During heating, the Na^+ and Mg^{2+} ions present in the residue are incorporated into the HAp crystal lattice to form a substituted Hap (Ptacek, 2016); this phase is thermally more stable than the initial HAp. The less stabilised fraction of HAp undergoes dehydroxylation and subsequent decomposition to form β-tricalcium phosphate (β-TCP). However, this decomposition phase also incorporates Na^+ and Mg^{2+} to stabilise its lattice, resulting in the formation of a complex calcium phosphate. Despite partial dehydroxylation, the decomposition temperature of the substituted HAp shifts to a higher temperature range. At 1250 °C, the temperature necessary for its complete decomposition to β-TCP is not reached, allowing it to persist. Goldberg et al. (Goldberg et al., 2020) found that apatite decomposition can begin at 850 °C, with α-TCP peaks detected at 1000 °C. Therefore, the coexistence of apatite and β-TCP in samples fired at 1250 °C is the result of incomplete decomposition. In addition to these phosphate phases, XRD analysis reveals the presence of anorthite ($CaAl_2Si_2O_8$, PDF 52–1344). This is due to the high availability of CaO in the HApW and the presence of SiO_2 and Al_2O_3 in the clay A. Anorthite is a characteristic reaction product in calcium-rich ceramic systems, formed from the reaction of CaO with clay components at temperatures of approximately 1150 °C (Sokolar and Nguyen, 2024).

As the proportion of clay A in the mixtures increases, the evolution of the phases becomes evident in the diffractograms. This is driven by the $CaO/(Al_2O_3 + SiO_2)$ ratio in the composition. Starting with the 30A composition, a decrease in the substituted apatite peaks is observed, probably due to the accelerated decomposition kinetics and progressive dissolution of this phase caused by the addition of clay A. The fraction of substituted apatite stabilised by Na^+ and Mg^{2+} ions exceed its stability limit owing to the increased reactivity of the medium, which is partly caused by the increased fluxing oxides (K_2O and SiO_2) contributed by the clay. In this environment, the substituted apatite undergoes a more complete conversion to its most stable decomposition product, complex calcium phosphate ($Ca_9MgNa(PO_4)_7$), at 1250 °C. This explains the concurrent increase in this phase up to the 40A composition value. Simultaneously, the anorthite content increases up to 50A, even though the total percentage of CaO decreases with the lower HApW content in these compositions. This suggests that the crystallisation efficiency of the available calcium is increasing, which is probably driven by the release of amorphous calcium from HApW into the system during heating. From the 30A composition onwards, increasing clay fluxes accelerate the release of amorphous calcium, introducing highly reactive CaO into the medium (Goltsman and Yatsenko, 2024). This CaO is then available to react with SiO_2 and/or Al_2O_3 present in the clay.

Fig. 7 shows the compositions of the HApW and clay A and B mixtures in the SiO_2-Al_2O_3-CaO phase diagram. 20A falls within the lime (CaO) formation region, which explains the high intensity of the substituted apatite and complex calcium phosphate. The mineralogy of these compositions is governed by reactions between CaO and P_2O_5 to form phosphates before they react completely with Al_2O_3/SiO_2 in the clay. Theoretically, the 30A and 40A compositions fall within the primary crystallisation fields of larnite (Ca_2SiO_4) and gehlenite

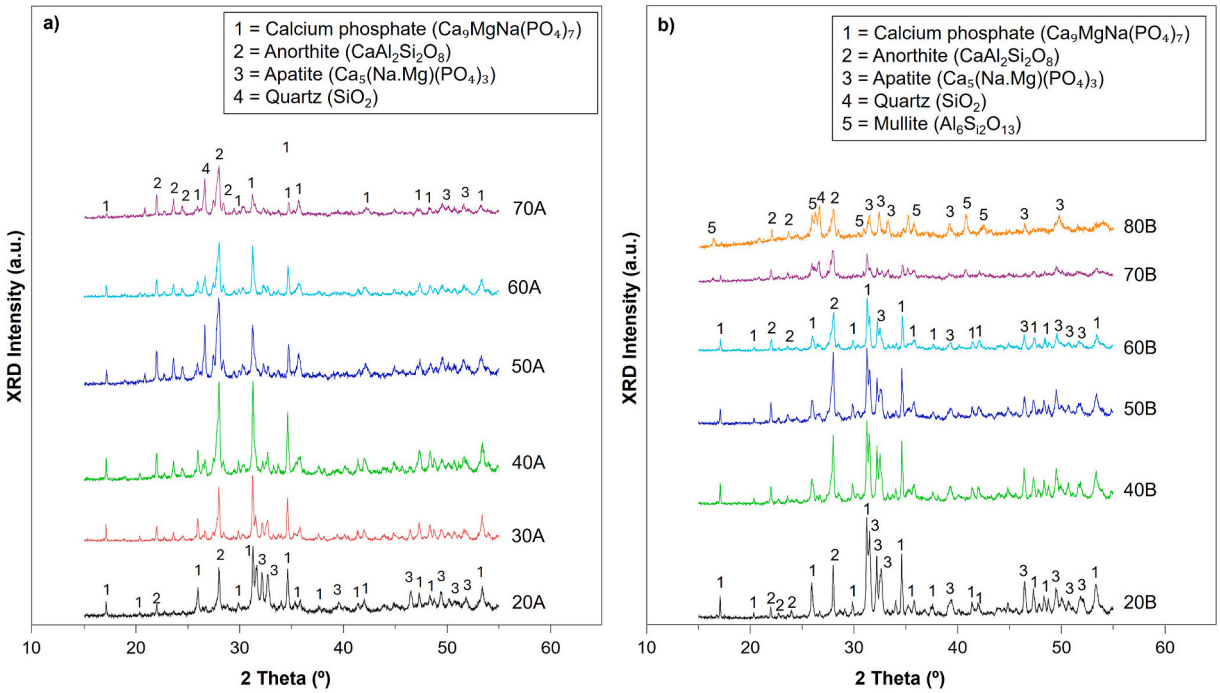

Fig. 6. XRD patterns for the hydroxyapatite residue (HApW) and a) Clay A fired at 1250 °C and b) Clay B fired at 1150 °C, showing the phases developed after firing, including Ca-phosphates, anorthite and mullite.

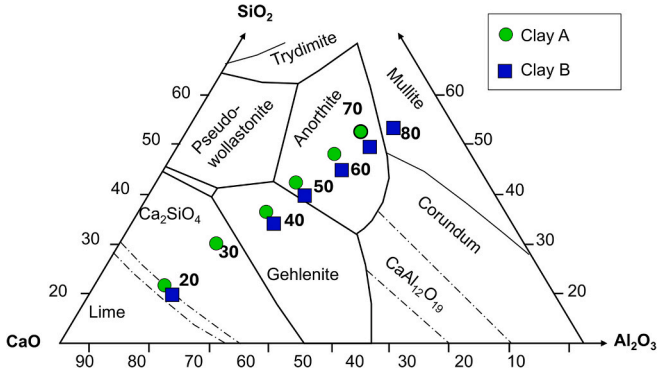

Fig. 7. Compositions of the HApW and clay A and B mixtures in the SiO_2-Al_2O_3-CaO phase diagram, showing their position relative to the primary crystallisation fields that help interpret the formation of anorthite, mullite and Ca–phosphate phases during firing.

($Ca_2Al_2SiO_7$). However, Fig. 7 shows that these phases did not develop during firing because of the competition for CaO. The formation of phosphate consumes a significant portion of the available CaO. This loss shifts the effective compositional point of the silicate-aluminate matrix away from the crystallisation fields of CaO-rich phases, such as larnite (Ca_2SiO_4) and gehlenite ($Ca_2Al_2SiO_7$), favouring the crystallisation of anorthite, which requires a lower CaO/(Al_2O_3 + SiO_2) ratio in the remaining system. Finally, the amount of anorthite decreases from the 60A composition, probably because the consumption of CaO to form phosphate shifts the composition towards the SiO_2/Al_2O_3-rich region of the ternary where mullite ($Al_6Si_2O_{13}$) occurs. However, the absence of detectable mullite in the XRD pattern can be attributed to kinetic factors. At 1250 °C, the thermal energy and dwell time are insufficient to overcome the activation barrier required for the nucleation of this crystalline phase, particularly in a high-viscosity matrix caused by excess SiO_2.

The phase evolution of mixtures containing clay B (fired at 1150 °C) exhibits greater kinetic efficiency in crystallisation than that observed in the clay A system (fired at 1250 °C). Compositions ranging from 20B to 60B exhibit an anorthite peak intensity comparable to that of their clay A system analogues, despite being fired at a lower temperature. One possible explanation is the higher proportion of fluxing agents in clay B. These oxides decrease the viscosity of the liquid phase at 1150 °C, accelerating ion diffusion and enabling anorthite to crystallise within its thermodynamic field (Chalouati et al., 2020). Additionally, mullite formation is observed in the 80B composition, likely due to the mineralising effect of Fe_2O_3 at such a low temperature.

However, from the 70B composition onwards, a decrease in the intensity of the anorthite peaks is observed, a trend that continues for 80B. This drop is due to competition for Al_2O_3 and SiO_2. Because 80B is located within the mullite field, where its formation is facilitated by the mineralising effect of Fe_2O_3 (Sadli et al., 2024), mullite becomes the dominant phase and consumes a significant proportion of the available Al_2O_3. This inhibits the crystallisation of anorthite, resulting in the remaining SiO_2 segregating from the liquid phase and crystallising as quartz. This explains the significant increase in quartz from the 70B composition.

It should be noted that the mineralogical evolution observed in the mixtures is also strongly influenced by the transformations of the clay matrices. During firing, kaolinite and muscovite in both clays undergo dehydroxylation and structural collapse, providing the aluminosilicate framework that favours the crystallisation of anorthite in both systems and mullite in the clay B compositions. These clay-derived transformations, together with the reactivity of the HApW phases, jointly determine the final phase assemblage observed in the fired products.

3.4. Pore size distribution and flexural strength of the new materials

Figs. 8 and 9 show the pore size distributions of the different compositions formulated with A and B clays, respectively. Composition 20A has a relatively narrow pore size distribution centred on small and intermediate diameters (mainly between 0.3 and 0.6 mm), with over 80 % of the pores measuring less than 0.6 mm. As the percentage of clay in the composition increases (50A and 60A), the distribution broadens and

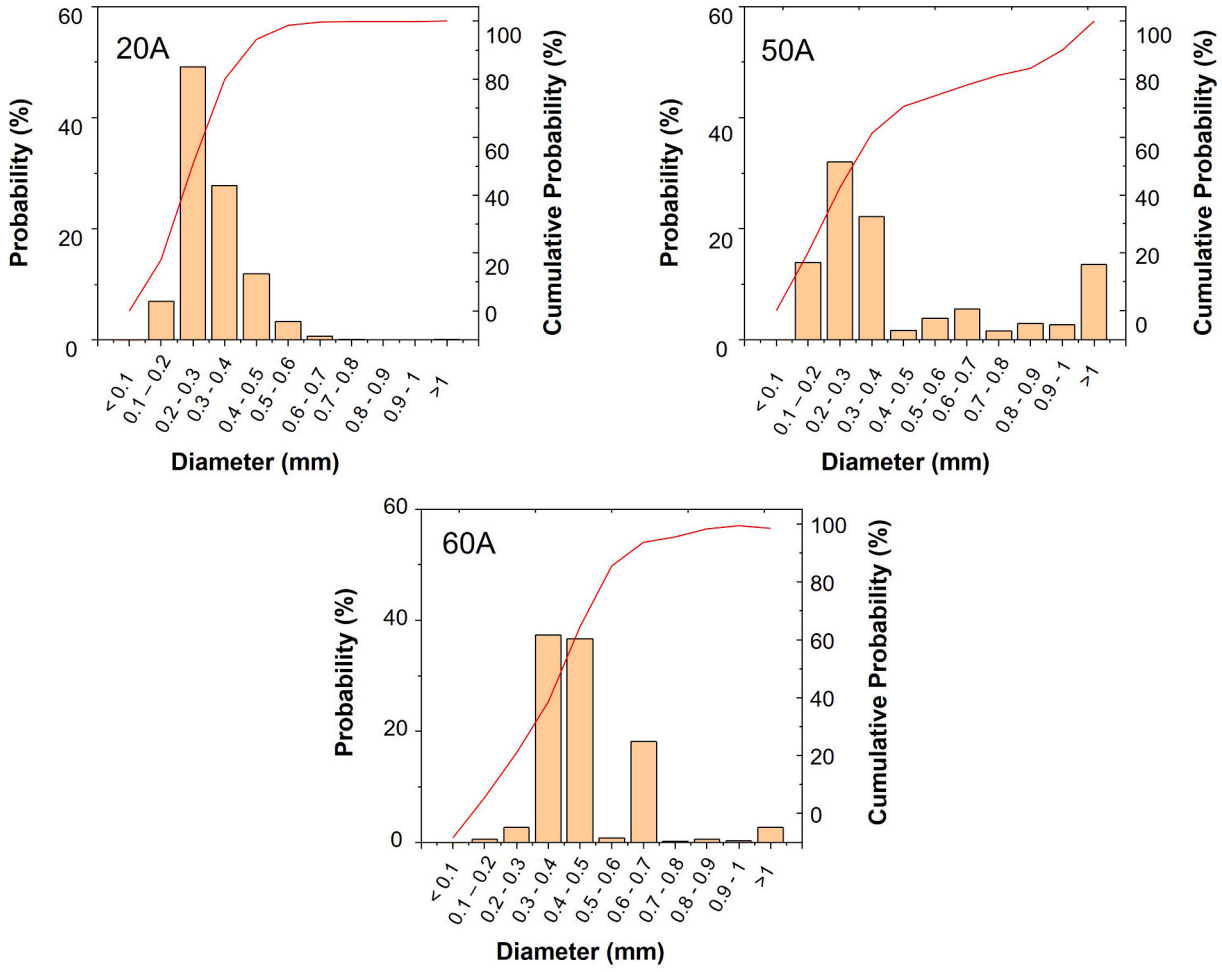

Fig. 8. Pore size distribution of the studied compositions formulated with clay A, showing broader and multimodal pore populations, especially at high HApW content.

becomes multimodal. While there is still a significant contribution from small pores (between 0.3 and 0.5 mm), a higher proportion of large pores (greater than 0.8 mm) is evident. This pore size distribution confirms the narrow sintering window of this system. However, this trend is counterintuitive. A higher HApW content is expected to produce larger pores. The 20B composition shows an extremely narrow distribution, with a main peak at approximately 0.8–0.9 mm. As the clay percentage in the mixtures increases (to 60B and 70B), the distribution narrows further and shifts towards smaller sizes (between 0.4 and 0.7 mm). The pore distribution of the compositions containing clay B is homogeneous and unimodal across the entire range of compositions. This contrasts with the dispersion and macropores of the A system, even when their compositions are similar. This is due to the greater effectiveness of the clay B fluxes in generating a low-viscosity liquid phase at 1150 °C (Zheng et al., 2025). This allows for rapid and uniform mass transport, efficiently eliminating pores.

Fig. 10 shows the total porosity and average pore size of the studied compositions. In mixtures with the clay B, porosity remains extremely low across the entire range, varying between 0.1 % and 0.4 %. In contrast, the porosity of the mixtures with clay A is significantly higher, ranging from 0.3 to 3.5 %. Porosity tends to be higher when the clay content is low (20A), after which it decreases, remaining in the range of 2.0–2.5 % for compositions with a higher clay content (50A and 60A). The higher overall porosity in the clay A system (despite the higher firing temperature) indicates a lower sintering efficiency in this system.

In terms of average pore size, the clay B mixtures consistently have a smaller average pore size (approx. 0.3 mm) than the clay A system. This is consistent with the narrow distribution observed in Fig. 9, and the low-viscosity liquid phase promotes densification by closing the pores without allowing them to grow. The average pore size is larger and more variable in mixtures with clay A, reaching a maximum of almost 0.5 mm. These results regarding porosity and pore size reinforce the conclusions drawn from the sintering study performed using heating microscopy (Fig. 5). This study showed that the clay B system had a more controlled densification profile and a greater ability to maintain its structural integrity at high temperatures. This is confirmed by the remarkably low total porosity and homogeneous, small-pore microstructure. Clay A, on the other hand, leads to the formation of liquid phases with a lower eutectic point or higher viscosity (due to the higher proportion of SiO_2). This results in a narrower sintering window and a more abrupt collapse, resulting in higher residual porosity and a wider pore size distribution (including macropores) in the final product.

Fig. 11 shows the flexural strength (σ_f) of the studied compositions and Fig. 12 illustrates the impact of porosity and pore size on σ_f. The mechanical strength of ceramic materials is determined by the total porosity and the size of the largest pore, which is considered the critical defect. The flexural strength results show that the limiting factor for strength differs between the two clay systems. In materials formulated with clay A, the strength increases linearly with decreasing HApW content, confirming that the total porosity is the primary limiting factor in this system. Consequently, the 20A composition exhibits the lowest σ_f (14 MPa), consistent with its maximum total porosity of 3.5 %. However, its high flux content results in oversintering at 1200 °C, where excess liquid phase traps the decomposition gases, leaving a high

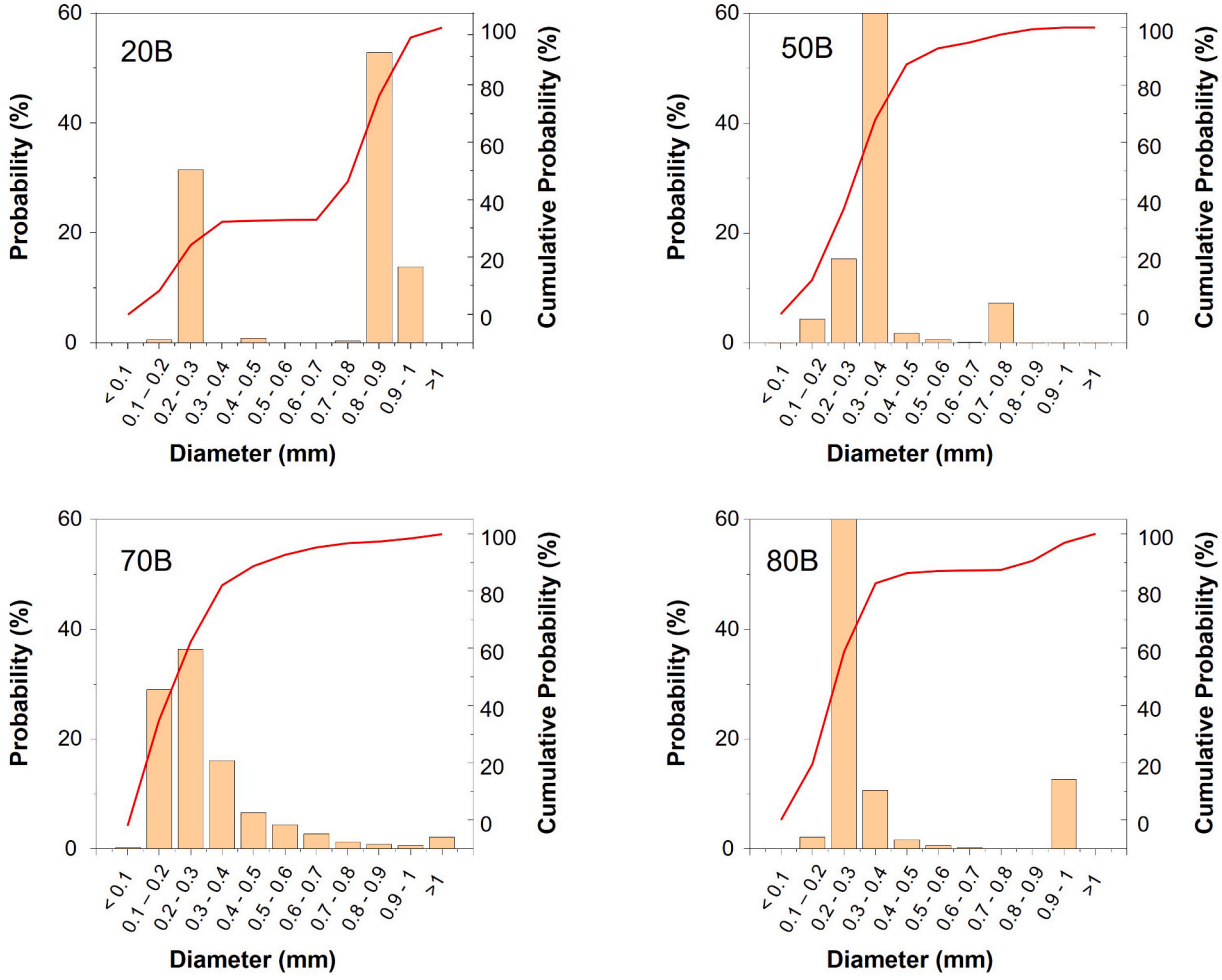

Fig. 9. Pore size distribution of the studied compositions formulated with clay B, showing narrow and homogeneous pore populations across compositions.

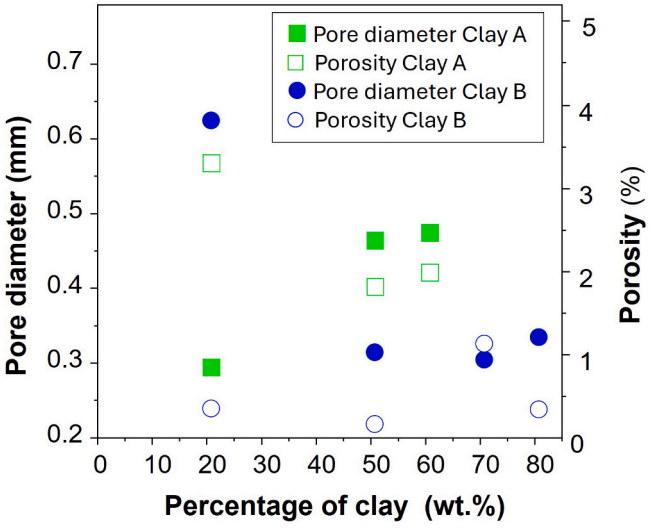

Fig. 10. Total porosity and average pore size of HApW and clay B mixtures, fired at 1200 °C, comparing the higher residual porosity in clay A with the dense bodies formed with clay B.

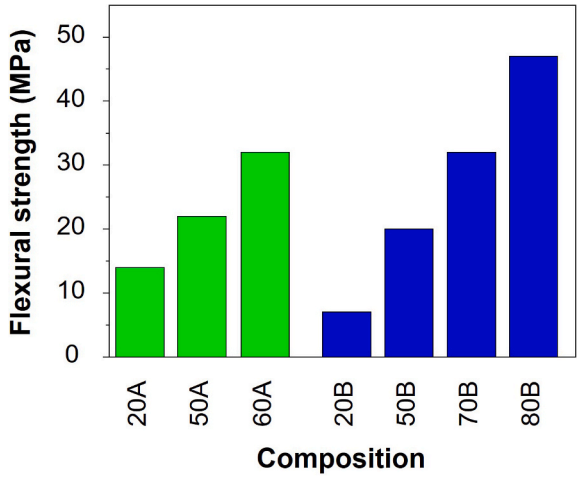

Fig. 11. Flexural strength of ceramic compositions, showing the progressive increase in strength with decreasing HApW content in clay A and the much stronger compositional dependence observed in clay B, where σ_f ranges from very low to the highest values obtained.

residual porosity that acts as a stress concentrator. σ_f increases significantly from 14 MPa (20A) to 32 MPa (60A) as the proportion of clay increases, stabilising the structural skeleton and facilitating more controlled densification. This reduces the total porosity to approximately 2 %.

In contrast to the clay A system, materials formulated with clay B exhibit minimal and constant total porosity ($\leq$ 0.4 %) across all compositions, suggesting that the strength should be high. However, σf

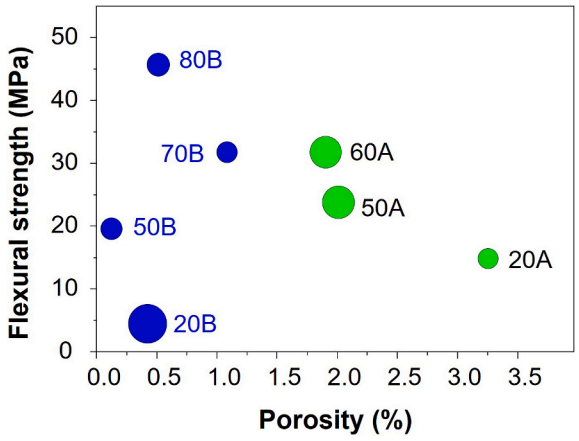

Fig. 12. Impact of porosity and pore size on the flexural strength of ceramic compositions, showing that compositions with larger critical pores exhibit lower flexural strength, while those with smaller and more uniform pores achieve higher σ_f values.

varies dramatically from 7 to 47 MPa, indicating that it is controlled by the quality of the microstructure (i.e., defect size) and the nature of the glass matrix. Composition 20B exhibits the lowest total porosity but the largest average pore size (approximately 0.85 mm). This combination explains the anomalously low σ_f of 7 MPa observed. High concentrations of HApW flux (80 %) and clay B fluxes promote densification, but they also accelerate the Ostwald ripening of residual pores (Singh et al., 2022). The result is a material that is almost completely dense yet still contains a small number of giant pores. According to fracture mechanics, the strength is inversely proportional to the square root of the critical defect size. These large pores act as stress concentrators, initiating fractures and counteracting the advantage of low volumetric porosity (Liao et al., 2025). The σ_f increases steadily as the proportion of HApW decreases, reaching a maximum value of 47 MPa for the 80B composition. The combination of low porosity and small, homogeneous pore size eliminates critical defects and ensures high strength. In addition, the crystalline matrix is enriched with mullite, as observed by XRD. Mullite is renowned for its exceptional hardness, high elastic modulus, and outstanding thermal stability. It usually forms acicular (needle-shaped) crystals, particularly when its formation is promoted by the fluxes. The formation of acicular mullite crystals in the glass matrix provides a reinforcement mechanism through interlocking and crack-deflection. Cracks encounter the edges of the needles, which deflects their path and consumes energy, significantly increasing the flexural strength (Cui et al., 2020).

These observations suggest that the dominant failure mechanisms differ between the two systems. In clay A compositions, fracture is predominantly controlled by weak glassy interphases and residual pores formed during sintering. In contrast, in clay B compositions, flexural strength is dictated by pore size, with critical defects dominating failure in high-HApW mixtures. However, when pore coarsening is avoided, the formation of acicular mullite in clay B promotes crack deflection and efficient load transfer. This explains the high σ_f values obtained for the most balanced formulations.

To evaluate the industrial feasibility of the ceramic materials developed, their flexural strength values were compared to the requirements of the ISO 13006:2018 “Ceramic tiles – Definitions, classification, characteristics and marking” standard. The compositions formulated with clay A correspond to Group BIIa, which has a minimum flexural strength requirement of 22 $N{\cdot}mm^{-2}$. Both 50A and 60A satisfy this requirement. Products in Group BIIa are typically suitable for indoor flooring in residential or commercial environments. Formulations incorporating Clay B fall within Group BIb, which requires a minimum flexural strength of 30 $N{\cdot}mm^{-2}$. Compositions 70B and 80B comply with this threshold and are therefore also appropriate for indoor floor tiles. Composition 50B meets the mechanical performance criteria for Group BIIb, while 20A corresponds to Group BIII. Both groups are commonly used for interior wall coverings in residential or commercial buildings. Finally, composition 20B does not meet the minimum strength required for any UNE-EN 14,411 category. These results demonstrate that several HApW-based formulations meet industrial performance standards and are suitable for real ceramic applications, depending on the clay matrix and HApW content.

Overall, the differences observed in densification, pore structure and mechanical behaviour between the two systems can be directly explained by their distinct chemical and mineralogical compositions, which determine their fluxing behaviour and sintering kinetics.

When compared with previous studies involving hydroxyapatite-containing wastes, clear differences can be seen. Bih et al. (2022) reported that bone ash additions (5–15 wt%) enhanced compressive strength by promoting cementitious reactions at 600–900 °C; however, they did not induce strong liquid-phase sintering or abrupt shrinkage. Similarly, Avelino et al. (2023) demonstrated that minor additions of synthetic hydroxyapatite (5–20 wt%) improved the mechanical performance of porcelain tiles via gradual densification and reduced porosity; there was no indication of premature melting. Loutou et al. (2017) studied phosphate sludge that exhibited partial fluorapatite decomposition and gehlenite formation. Sintering was controlled by limited melt flow, which occurred at 900–1000 °C, with optimal behaviour occurring at 1152 °C. In contrast, the HApW used in the present study contains crystalline HAp, amorphous calcium phosphate, and reactive impurities (Na_2O, MgO, and SO_3). These impurities collectively promote intense and early liquid-phase formation. This results in significantly sharper shrinkage, a narrower sintering window and a stronger effect on pore elimination or coarsening, depending on the clay matrix. These compositional and kinetic differences explain the distinct mineralogical evolution and microstructural features observed in HApW-based ceramics, as well as the differences in mechanical behaviour compared with that of previously investigated phosphate-rich wastes.

3.5. *Microstructural analysis of the new materials*

Fig. 13 shows the results of the microstructural analysis of 60A sample, which was performed using FESEM/EDS. Elemental mapping analysis reveals a heterogeneous microstructure resulting from complex sintering reactions. The main matrix consists of an interconnected network of silicon and aluminium, and EDS analysis indicates the formation of calcium aluminosilicates. This distribution is highly consistent with the non-stoichiometric anorthite phase previously identified by XRD. However, FESEM observations of the matrix do not reveal any sharp, euhedral, or prismatic crystalline forms that would enable the visual identification of anorthite crystals. The lack of a well-defined crystalline morphology is primarily due to the crystallisation kinetics. The high viscosity of the liquid phase in this system inhibits ionic mobility, preventing the anorthite crystals from growing to a visible size. Additionally, the substantial amorphous glassy phase envelops the small crystals and their irregular boundaries, creating the appearance of a fused matrix rather than an assembly of discrete crystals.

This aluminosilicate matrix contains two types of inclusions. Phosphorus is concentrated in discrete, scattered clusters that correspond to calcium phosphates derived from HApW. Similarly, silicon nuclei indicate the presence of residual quartz grains from clay due to an incomplete reaction.

Higher-magnification micrographs of the calcium phosphate region reveal a microstructure composed of dense, agglomerated aggregates of irregularly shaped particles ranging in size from the nanometre to submicrometre scale. These particles do not exhibit well-defined crystalline faces but instead appear as strongly cohesive globular or irregular nodules. This morphology could be due to massive nucleation, that is, a high density of phosphate nuclei that grow rapidly, but in a disordered

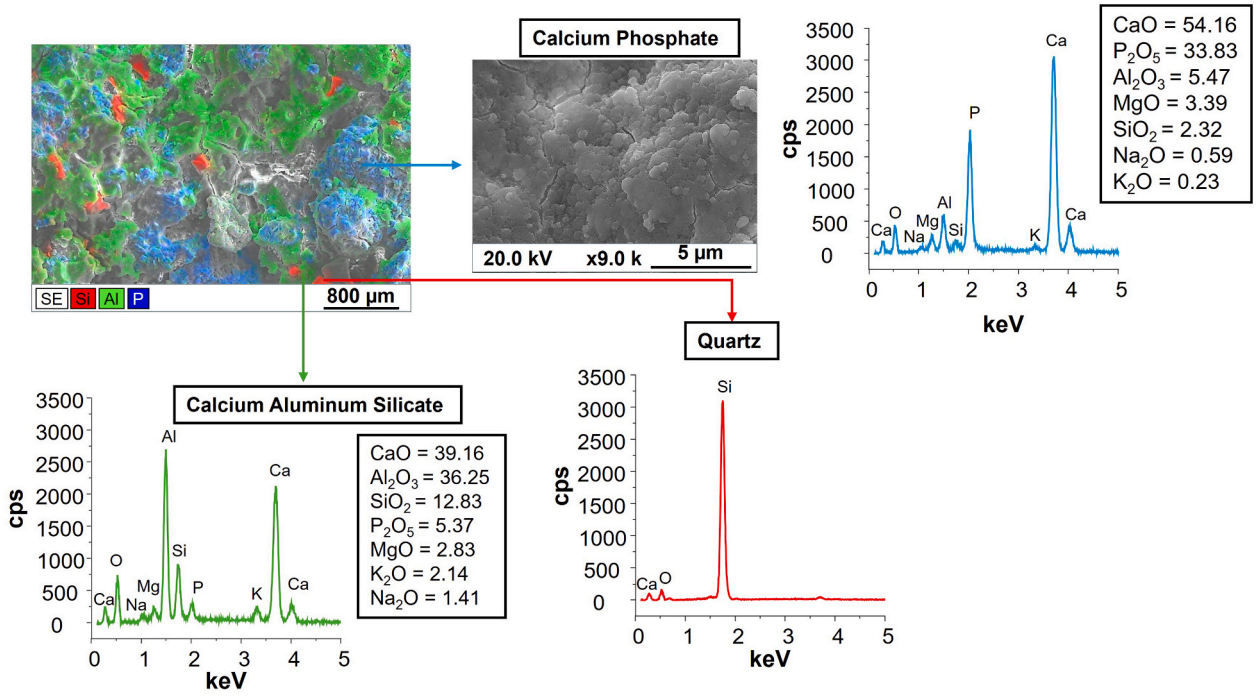

Fig. 13. Microstructural analysis of sample 60A, performed using FESEM/EDS, showing a glassy aluminosilicate matrix containing Ca–phosphate clusters and heterogeneous pores.

and agglomerated manner without developing into large crystalline structures. The texture is porous at the nanometric scale, with small, interconnected pores visible between the particles that constitute the aggregates. In terms of strength, this region can act as a local weak point.

Fig. 14 shows the microstructural analysis of the composition 80B. The low-magnification micrograph reveals a microstructure characterised by a dense aluminosilicate matrix that is less porous than that observed in composition 60A, together with a phosphate phase (apatite) dispersed into small grains and significantly better integrated into the matrix than in the clay A system. This greater densification is attributed to the formation of a low-viscosity liquid phase, which is facilitated by clay B clay fluxes and allows for effective pore closure. Fig. 15 shows a high-magnification FESEM image in which acicular mullite crystals are clearly visible. These acicular crystals provide internal structural reinforcement to the densified matrix. The main mechanisms are crack deflection and interlocking. When a microcrack propagates through the material under stress, it encounters mullite needles, which deflect its path and cause it to consume additional energy. This dramatically increases the toughness and, therefore, the flexural strength (Cui et al., 2020).

Overall, the thermal, mineralogical, densification and microstructural results provide a coherent explanation of the sintering mechanism for the HApW–clay systems. During heating, the amorphous calcium-phosphate fraction within the HApW dehydrates and progressively reorganises. It crystallises at temperatures between 880 and 900 °C, which promotes the formation of a reactive calcium-phosphate melt once the HAp begins to dehydroxylate above ~ 1080 °C. The interaction of this melt with the clay matrices determines the distinct behaviour of the two systems. Clay A, characterised by a high SiO_2/Al_2O_3 ratio and low flux content, generates a comparatively viscous liquid that limits ion mobility and favours the development of an amorphous aluminosilicate matrix with embedded Ca-phosphate particles. In contrast, clay B, which is richer in Fe_2O_3 and K_2O, produces a liquid phase with significantly lower viscosity that enhances mass transport. This enables earlier pore closure, the formation of well-crystallised anorthite and mullite, and ultimately a more homogeneous and mechanically robust

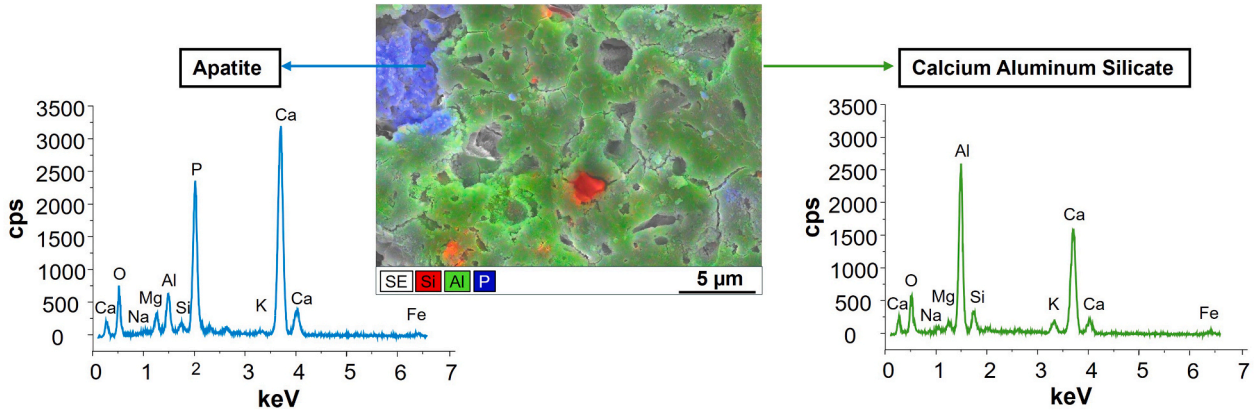

Fig. 14. Microstructural analysis of sample 80B, performed using FESEM/EDS, showing a dense matrix with well–integrated Ca–phosphate phases and mullite development.

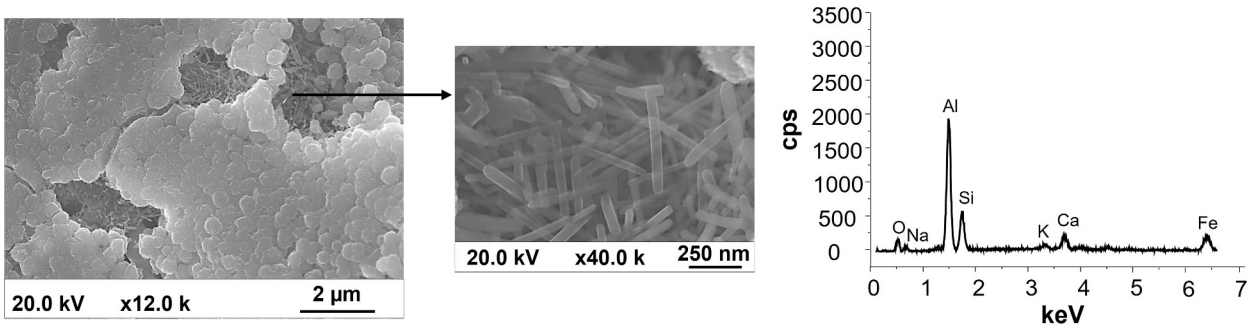

Fig. 15. Microstructural analysis of sample 80B, performed using FESEM/EDS, showing well–developed acicular mullite crystals embedded within a dense ceramic matrix.

microstructure. These transformations can be summarised as follows: initial reorganisation of the amorphous calcium-phosphate fraction, crystallisation, formation of the liquid phase, and subsequent densification and phase development. These steps lead to the observed differences in sintering temperatures and technological properties between the two HApW-clay systems.

3.6. Environmental impact

Fig. 16 shows the results of the leaching test conducted to the ceramic samples and HApW compared to the limit values of the Decree 646/2020, which establish the threshold of the concentrations of contaminants in the leachate for landfill admission (Royal Decree 646/2020). The leaching test was therefore conducted following the UNE-EN_12457-4 standard previously described in section 2.4. The threshold values considered correspond to the "Inert Waste" category established in Royal Decree 646/2020 (Annex II), which establishes maximum leachate concentrations of 500, 30, 40, 2000, 400, 500 and 4000 $\mu g \cdot L^{-1}$ for As, Cd, Cr, Cu, Ni, Pb and Zn, respectively.

All analysed samples showed concentrations well below these regulatory thresholds. The highest values measured were 1.72, 0.0025, 0.07, 0.23, 0.67, 0.005, and 3.30 $\mu g \cdot L^{-1}$ for As, Cd, Cr, Cu, Ni, Pb, and Zn, respectively. These values were at least 3 orders of magnitude below their respective limit values. Considering that the Inert Waste category represents the most restrictive classification for landfill acceptance, these results confirm the high stability of the developed ceramics and its effective immobilization capacity for the elements of concern.

Comparison with other studies is challenging, and to the best of our knowledge, the substitution of clay with contaminated hydroxyapatite in ceramics has not been studied. However, several studies have explored the partial or total substitution of clay with various industrial or agricultural residues to produce ceramics. For example, the addition of phosphogypsum waste in ceramic bodies has been shown to improve technological properties of fired ceramic tiles, with toxicity characteristic leaching procedure (TCLP) results indicating negligible environmental impact under standard protocols (Contreras et al., 2018). In the same way, the solidification for Cr, Cu, Zn, As, and Pb into sludge bricks obtained by mixing sewage sludge with shale was showed to be feasible in recent research (Zhang et al., 2015). In that study, the leachate toxicity was proved to be lower than that of national standards. Despite the methodological and compositional differences, (Karayannis et al., 2016) concluded in a recent review that stabilization/solidification of potentially hazardous heavy metals from solid wastes (including power station ashes, steelmaking by-products, various metallurgical wastes, and sewage sludges) into clay-based ceramics was feasible. In addition, relatively low lixiviation levels, as concentrations of these elements in the leachates were reported to remain within acceptable limits, thus providing an alternative to minimize the environmental impacts.

Two mechanisms may be attributed to explain this observation:

Chemical stabilization

The possible incorporation of metal cations into newly formed phosphate and apatite-type phases. Apatite-type phosphates can incorporate divalent and trivalent metal cations in the chemical structure. Apatite and related phosphate phases are widely used or proposed for in-situ immobilization of Cu, Ni, Pb, Cd, Zn and other metals because of this capacity (Feng et al., 2010; Kato et al., 2023; Mavropoulos et al., 2002). Another possibility is that the heavy metals could react with other components to form a new crystal compound (Guo et al., 2017), however, in the XRD there are no visible peaks of any heavy metals phase, probably because of the low concentrations of these elements in the material.

Physical stabilization

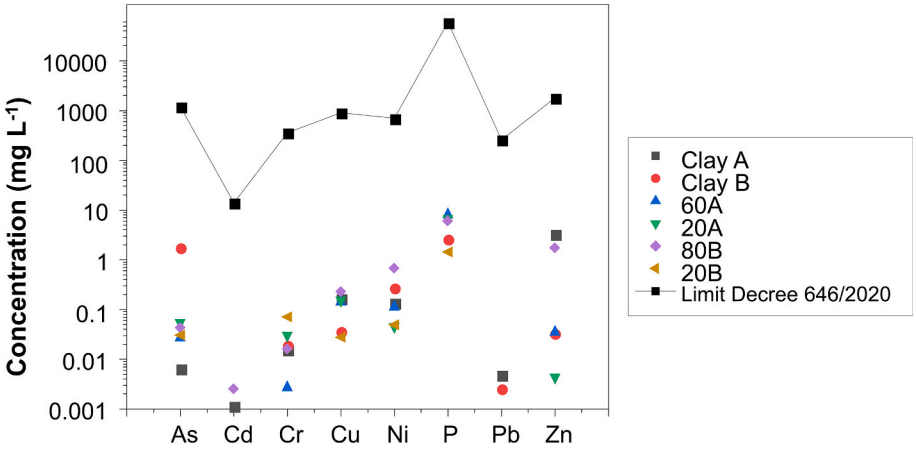

Fig. 16. Leaching test concentrations of ceramic compositions and Limit Decree 646/2020 thresholds.

The possible physical encapsulation within an essentially dense silicate/aluminosilicate matrix (Yuan et al., 2023). In addition, reduced accessible surface area and transport due to very low total porosity (< 3.5 %) observed in all compositions therefore providing a strong physical barrier to contaminant release.

On the other hand, it should be noted that the HApW originates from the cleaning of a NORM (Naturally Occurring Radioactive Material) waste (Soto-Cruz et al., 2024). Therefore, assessing the potential radiological impact of this material is essential. As previously discussed in an earlier study in which we valorised another residue derived from the cleaning of PGL (Soto-Cruz et al., 2025), the radionuclides present in these wastes do not pose a significant concern regarding external radiation exposure. This is because, in the equation used to calculate the radiological index on which this assessment is based (Index *I*), the radionuclides found in the highest concentrations in our samples are not included. The activity concentration index (*I*) functions as a regulatory parameter to verify compliance with radiation safety limits, ensuring that external gamma exposure from construction materials remains within the annual threshold of 1 mSv. This requirement, stipulated in Article 75(1) of the 2013/59/EURATOM Directive, provides a standardised approach to control potential radiological risks associated with building materials. This index should not exceed the value of unity ($I \leq 1$) for materials used in bulk amounts, to ensure that the additional external dose received by occupants living in buildings constructed with these materials does not exceed the reference value of 1 mSv· year^{-1} (Llanes et al., 2018). In this case, the main radionuclide present was ^{238}U, which is not considered in the index equation due to its alpha-emitting nature. Anyway, the index (*I*) was calculated for the ceramics with the higher composition of HApW following the Eq. (1):

$$I = \frac{C_{226Ra}}{300} + \frac{C_{232Th}}{200} + \frac{C_{40K}}{3000} \quad (1)$$

where C_{226Ra}, C_{232Th} and C_{40K} are the activity concentrations for ^{226}Ra, ^{232}Th and ^{40}K, respectively, expressed in Bq·kg^{-1}. The results were consistent with the previous discussion, as the index *I* for the sample 20B was 0.24, which is less than 1, and it is comparable to other building materials such as ordinary Portland cement ($I = 0.25$) (Soto-Cruz et al., 2025b).

Nevertheless, the potential environmental impact associated with its use must be considered. For this reason, the activity concentration of this radionuclide was measured in the leachates obtained from the leaching test. The results showed that the activity was < 0.2 Bq·L^{-1} in all samples. To ensure the radiological safety of these leachates, the indicative dose established by Spanish regulation Royal Decree 314/2016 was calculated. The indicative dose represents the estimated radiation dose that a person would receive from drinking such water over one year and serves as a benchmark for radiological safety assessment. Based on the measured values (0.2 Bq·L^{-1} for ^{238}U), the calculated indicative dose for the leachates was < 0.1 mSv·year^{-1}. Consequently, the environmental impact can be considered negligible.

While the present study demonstrates that the developed clay-based ceramics effectively immobilize heavy metals and ^{238}U under the tested conditions, the long-term stability under environmental ageing or weathering was not directly assessed. Factors such as repeated wet-dry cycles, freeze–thaw, or acidic conditions could potentially influence the leaching behaviour over extended periods. Therefore, further studies including accelerated ageing tests or long-term field trials are needed to fully confirm durability under realistic environmental conditions. From a technical perspective, the processing route employed (mixing, shaping, and conventional ceramic sintering) relies on well-established industrial technologies, suggesting that large-scale implementation is feasible. However, full-scale deployment would require careful evaluation of energy consumption, emissions, and process optimization to ensure environmental and economic viability within a life cycle framework. In this context, occupational radiological exposure must be carefully evaluated in a scale-up scenario, particularly regarding potential internal exposure through inhalation of fine particulate matter during handling, grinding, or mixing stages due to the high ^{238}U activity concentration.

4. Conclusions

The study confirms the technical feasibility of valorising the waste (HApW) derived from phosphogypsum leachate treatment as a secondary raw material in ceramic formulations. Thermal analysis showed that HApW undergoes a sequence of transformations associated with the crystallization of amorphous calcium phosphate, dehydroxylation of hydroxyapatite, and subsequent liquid-phase formation at higher temperatures.

Heating microscopy established optimal firing temperatures of 1150 °C for systems containing clay B and 1250 °C for those with clay A, ensuring adequate densification without deformation. At high HApW contents, the mineralogy was dominated by phases derived from the residue, mainly substituted apatite ($Ca_5(Na,Mg)(PO_4)_3$) and complex calcium phosphate ($Ca_9MgNa(PO_4)_7$), resulting from thermal decomposition. The incorporation of HApW promoted strong sintering and significant shrinkage, while the clay fraction acted as a stabilizing skeleton moderating these effects. The flexural strength of the fired bodies ranged from 7 to 47 MPa and decreased linearly with increasing HApW content; this behaviour was influenced by both total porosity and pore size distribution. Microstructural analysis confirmed the formation of heterogeneous matrices whose characteristics depend on the clay type and HApW content. In compositions with clay A, the high viscosity of the liquid phase limited crystal growth, leading to a predominantly amorphous, fused microstructure. In contrast, clay B promoted the development of a denser matrix with well-integrated apatite phases and acicular mullite crystals, which enhanced densification and contributed to improved mechanical performance through crack deflection and interlocking mechanisms. From an environmental standpoint, all measured contaminant concentrations were well below regulatory thresholds. The immobilization of metallic cations could be attributed to their incorporation into apatite or crystalline phases, and to physical encapsulation within the silicate/aluminosilicate matrix. The low porosity of the materials further reduced the accessible surface for contaminant transport. Moreover, radiological evaluation confirmed the absence of risk, with indicative doses below 0.1 mSv·year^{-1}. Based on the mechanical performance benchmarked against ISO 13006, compositions 50A and 60A meet the requirements for BIIa indoor floor tiles, while 70B and 80B satisfy BIb specifications, identifying these formulations as the most suitable ranges for practical ceramic applications. The processing route employed here is compatible with industrial fast-firing practice, and the high substitution levels achieved (up to 50–80 wt% HApW) indicate a realistic potential for significant annual waste utilisation in ceramic production, reinforcing the industrial relevance of the approach. It should also be noted that the applicability of the present results is conditioned by the specific firing temperatures and the use of the two commercial clays studied, which represent typical but not exhaustive ceramic matrices; nevertheless, the identified optimal compositions provide a realistic starting point for industrial implementation.

In the context of cleaner materials, this study demonstrates the successful valorisation of a waste derived from phosphogypsum leachate treatment (HApW) as a secondary raw material in ceramic production. This strategy contributes to cleaner material development by reducing waste accumulation, minimising potential pollutant release, and promoting circular material flows through the reuse of industrial by-products.

Future research could explore the optimisation of HApW incorporation below the ranges tested here, as well as its behaviour in other ceramic matrices or under alternative firing schedules, to further expand the potential applications of this residue. Any industrial implementation would require a deep radiological risk assessment to comply with

occupational radiological safety regulations. Overall, while the current work demonstrates technical feasibility and potential for waste valorisation, detailed techno-economic assessments, life cycle analyses, and radiological evaluations will be necessary in future studies to fully confirm scalability and practical implementation potential.

CRediT authorship contribution statement

F.J. Soto-Cruz: Writing – original draft, Resources, Methodology, Investigation, Data curation, Conceptualization. **A. López-Delgado:** Writing – review & editing, Formal analysis. **I. Ramos-Lerate:** Writing – original draft, Data curation. **J.P Bolívar:** Writing – review & editing, Supervision, Project administration, Investigation, Funding acquisition. **M.J. Gázquez:** Writing – review & editing, Supervision, Project administration, Methodology, Funding acquisition. **M. Romero:** Writing – original draft, Supervision, Methodology, Investigation, Formal analysis, Conceptualization.

Declaration of competing interest

The authors declare that they have no known competing financial interests or personal relationships that could have appeared to influence the work reported in this paper.

Acknowledgments

This research was funded by Grants PID2020–116461RB-C21 and 116461RA-C22 funded by MICIU/AEI/ 10.13039/501100011033; Research grant UCA/REC44VPCT/2021, by the University of Cádiz. The technical support of Ms. Esther Martín is recognised.

Data availability

Data will be made available on request.

References

Abu Hanifah, N.Z.H., Hashim, S., Halmat, J.H., Fahmi, M.R., Sanusi, M.S.M., Othman, N. K., 2023. Radiation hazard assessments of natural radioactivity in clay-based cosmetic products in Malaysia. Rad Phys Chem 202, 110583. https://doi.org/10.1016/j.radphyschem.2022.110583.

Avelino, F.P., de Araujo, W.M.P., Lima Soares, R.A., Peña-Garcia, R., Lobo, A.O., 2023. Porcelain Ceramic Tile Manufactured with the Addition of Hydroxyapatite in Ceramic Formulations. Minerals 13, 1120. https://doi.org/10.3390/min13091120.

Ayala, J., Fernández, B., 2020. Industrial waste materials as adsorbents for the removal of As and other toxic elements from an abandoned mine spoil heap leachate: a case study in Asturias. J. Hazard. Mater. 384, 121446. https://doi.org/10.1016/j.jhazmat.2019.121446.

Bih, N.L., Mahamat, A.A., Chinweze, C., Ayeni, O., Bidossèssi, H.J., Onwualu, P.A., Boakye, E.E., 2022. The effect of Bone Ash on the Physio-Chemical and Mechanical Properties of Clay Ceramic Bricks. Buildings 12, 336. https://doi.org/10.3390/buildings12030336.

Bilal, E., Bellefqih, H., Bourgier, V., Mazouz, H., Dumitraş, D.G., Bard, F., Laborde, M., Caspar, J.P., Guilhot, B., Iatan, E.L., Bounakhla, M., Iancu, M.A., Marincea, Ş., Essakhraoui, M., Li, B., Diwa, R.R., Ramirez, J.D., Chernysh, Y., Chubur, V., Roubík, H., Schmidt, H., Beniazza, R., Cánovas, C.R., Nieto, J.M., Haneklaus, N., 2023. Phosphogypsum circular economy considerations: a critical review from more than 65 storage sites worldwide. J. Clean. Prod. 414, 137561. https://doi.org/10.1016/J.JCLEPRO.2023.137561.

Bolívar, J.P., García-Tenorio, R., Mas, J., 1998. Radioactivity of phosphogypsum in the south-west of Spain. Radiat. Prot. Dosim. 76, 185–189. https://doi.org/10.1093/oxfordjournals.rpd.a032263.

Bulina, N.V., Makarova, S.V., Baev, S.G., Matvienko, A.A., Gerasimov, K.B., Logutenko, O.A., Bystrov, V.S., 2021. A Study of thermal Stability of Hydroxyapatite. Minerals 11, 1310. https://doi.org/10.3390/min11121310.

Cao, X., Harris, W.G., Josan, M.S., Nair, V.D., 2007. Inhibition of calcium phosphate precipitation under environmentally-relevant conditions. Sci. Total Environ. 383, 205–215. https://doi.org/10.1016/j.scitotenv.2007.05.012.

Chalouati, Y., Bennour, A., Mannai, F., Srasra, E., 2020. Characterization, thermal behaviour and firing properties of clay materials from Cap Bon Basin, north-east Tunisia, for ceramic applications. Clay Miner. 55, 351–365. https://doi.org/10.1180/clm.2021.4.

Chernysh, Y., Yakhnenko, O., Chubur, V., Roubík, H., 2021. Phosphogypsum Recycling: A Review of Environmental Issues, Current Trends, and Prospects. Applied Sciences 2021, Vol. 11, Page 1575 11, 1575. https://doi.org/10.3390/APP11041575.

Cui, K., Zhang, Y., Fu, T., Wang, J., Zhang, X., 2020. Toughening Mechanism of Mullite Matrix Composites: a Review. Coatings 10, 672. https://doi.org/10.3390/coatings10070672.

Contreras, M., Teixeira, S.R., Santos, G.T.A., Gázquez, M.J., Romero, M., Bolívar, J.P., 2018. Influence of the addition of phosphogypsum on some properties of ceramic tiles. Constr. Build. Mater. 175, 588–600. https://doi.org/10.1016/j.conbuildmat.2018.04.131.

Feng, Y., Gong, J.-L., Zeng, G.-M., Niu, Q.-Y., Zhang, H.-Y., Niu, C.-G., Deng, J.-H., Yan, M., 2010. Adsorption of Cd (II) and Zn (II) from aqueous solutions using magnetic hydroxyapatite nanoparticles as adsorbents. Chem. Eng. J. 162, 487–494. https://doi.org/10.1016/j.cej.2010.05.049.

Galindo, C., Mougin, L., Fakhi, S., Nourreddine, A., Lamghari, A., Hannache, H., 2007. Distribution of naturally occurring radionuclides (U, Th) in Timahdit black shale (Morocco). J. Environ. Radioact. 92, 41–54. https://doi.org/10.1016/j.jenvrad.2006.09.005.

Gázquez, M.J., Mantero, J., Mosqueda, F., Bolívar, J.P., García-Tenorio, R., 2014. Radioactive characterization of leachates and efflorescences in the neighbouring areas of a phosphogypsum disposal site as a preliminary step before its restoration. J. Environ. Radioact. 137, 79–87. https://doi.org/10.1016/J.JENVRAD.2014.06.025.

Gázquez, M.J., Paz Gómez, D.C., Alonso, J.J., Pérez-Moreno, S.M., Ramos-Lerate, I., Ruiz, M.C.-, Bolívar, J.P.,, 2022. A new methodology based on TRU resin to measure U-, Th-isotopes and 210Po by alpha-particle spectrometry. Talanta 253, 123972. https://doi.org/10.1016/J.TALANTA.2022.123972.

Goldberg, M.A., Protsenko, P.V., Smirnov, V.V., Antonova, O.S., Smirnov, S.V., Konovalov, A.A., Vorckachev, K.G., Kudryavtsev, E.A., Barinov, S.M., Komlev, V.S., 2020. The enhancement of hydroxyapatite thermal stability by Al doping. J. Mater. Res. Technol. 9, 76–88. https://doi.org/10.1016/j.jmrt.2019.10.032.

Goltsman, B.M., Yatsenko, E.A., 2024. Modern fluxing materials and analysis of their impact on silicate structures: a review. Open Ceram. 17, 100540. https://doi.org/10.1016/j.oceram.2024.100540.

Guerrero, J.L., Pérez-Moreno, S.M., Gutiérrez-Álvarez, I., Gázquez, M.J., Bolívar, J.P., 2021. Behaviour of heavy metals and natural radionuclides in the mixing of phosphogypsum leachates with seawater. Environ. Pollut. 268, 115843. https://doi.org/10.1016/J.ENVPOL.2020.115843.

Guo, B., Liu, B., Yang, J., Zhang, S., 2017. The mechanisms of heavy metal immobilization by cementitious material treatments and thermal treatments: a review. J. Environ. Manage. 193, 410–422. https://doi.org/10.1016/j.jenvman.2017.02.026.

Ibrahim, E.M., 2024. The 234U/238U activity ratio as an indicator of redox surface in the Allouga Quarry face, Southwestern Sinai. Egypt. J Radioanal Nucl Chem 333, 5831–5844. https://doi.org/10.1007/s10967-024-09662-9.

Indurkar, A., Choudhary, R., Rubenis, K., Locs, J., 2021. Advances in Sintering Techniques for Calcium Phosphates Ceramics. Materials 14, 6133. https://doi.org/10.3390/ma14206133.

Kalendova, A., Kupkova, J., Urbaskova, M., Merinska, D., 2024. Applications of clays in nanocomposites and ceramics. Minerals 14, 93. https://doi.org/10.3390/min14010093.

Karayannis, V.G., Karapanagioti, H.K., Domopoulou, A.E., Komilis, D.P., 2016. Stabilization/Solidification of Hazardous Metals from Solid Wastes into Ceramics. Waste and Biomass Valorization 2016 8:5 8, 1863–1874. https://doi.org/10.1007/s12649-016-9713-z.

Kato, S., Kagawa, S., Saito, K., Ogasawara, M., 2023. Incorporation and deposition behaviors of Cu and Ni ions into hydroxyapatite channels by heat treatment. J. Phys. Chem. Solid 177, 111287. https://doi.org/10.1016/j.jpcs.2023.111287.

Kingery, W.D., Bowen, H.K., Uhlmann, R., 1976. Introduction to Ceramics, 2nd ed. Wiley India, New Delhi.

Leder, N., Kumar, M., Rodrigues, V.S., 2020. Influential factors for value creation within the Circular Economy: Framework for Waste Valorisation. Resour. Conserv. Recycl. 158, 104804. https://doi.org/10.1016/j.resconrec.2020.104804.

Liao, Z., Rabiee, H., Ge, L., Li, X., Yang, Z., Xue, Q., Shen, C., Wang, H., 2025. Revealing pore microstructure impacts on the compressive strength of porous proppant based on finite and discrete element method. J. Mater. Sci. Technol. 211, 72–81. https://doi.org/10.1016/j.jmst.2024.05.054.

Lin, Y.-W., Peng, S.-Y., Lee, W.-H., Lin, Y.-Y., Hung, M.-J., Lin, K.-L., 2023. Characterization of Cu2+ adsorption for eco-hydroxyapatite derived from limestone sludge via hydrothermal synthesis. J Mater Cycles Waste Manag 25, 1069–1081. https://doi.org/10.1007/s10163-023-01593-z.

Ling, Z.S., Jaafar, M.H., Ismail, N., 2025. The knowledge, attitudes and practices in circular economy: a review of industrial waste management in China. Cleaner Waste Syst. 11, 100276. https://doi.org/10.1016/j.clwas.2025.100276.

Llanes, M.C., González, M.J.G., Moreno, S.M.P., Raya, J.P.B., 2018. Recovery of ilmenite mud as an additive in commercial Portland cements. Environ. Sci. Pollut. Res. 25, 24695–24703. https://doi.org/10.1007/S11356-018-2498-9/TABLES/7.

Loutou, M., Hajjaji, M., Babram, M.A., Mansori, M., Favotto, C., Hakkou, R., 2017. Phosphate sludge-based ceramics: Microstructure and effects of processing factors. Journal of Building Engineering 11, 48–55. https://doi.org/10.1016/j.jobe.2017.04.002.

Martín, M.I., Andreola, F., Barbieri, L., Bondioli, F., Lancellotti, I., Rincón, J.M., Romero, M., 2013. Crystallisation and microstructure of nepheline-forsterite glass-ceramics. Ceram. Int. 39, 2955–2966. https://doi.org/10.1016/j.ceramint.2012.09.072.

Mas, J.L., San Miguel, E.G., Bolívar, J.P., Vaca, F., Pérez-Moreno, J.P., 2006. An assay on the effect of preliminary restoration tasks applied to a large TENORM wastes disposal in the south-west of Spain. Sci. Total Environ. 364, 55–66. https://doi.org/10.1016/J.SCITOTENV.2005.11.006.

Mavropoulos, E., Rossi, A.M., Costa, A.M., Perez, C.A.C., Moreira, J.C., Saldanha, M., 2002. Studies on the Mechanisms of Lead Immobilization by Hydroxyapatite. Environ. Sci. Technol. 36, 1625–1629. https://doi.org/10.1021/es0155938.

Millán-Becerro, R., Pérez-López, R., Cánovas, C.R., Macías, F., León, R., 2023. Phosphogypsum weathering and implications for pollutant discharge into an estuary. J Hydrol (amst) 617, 128943. https://doi.org/10.1016/J.JHYDROL.2022.128943.

Millán-Becerro, R., Pérez-López, R., Macías, F., Cánovas, C.R., Papaslioti, E.M., Dolores Basallote, M., 2019. Assessment of metals mobility during the alkaline treatment of highly acid phosphogypsum leachates. Sci. Total Environ. 660, 395–405. https://doi.org/10.1016/J.SCITOTENV.2018.12.305.

Nakashima, K., Misawa, S., Kobayashi, Y., Ishigaki, T., Ishikawa, Y., Yin, S., Kakihana, M., Goto, T., Sekino, T., 2024. Atomic arrangement analysis and crystal growth mechanism of HAp nanocrystal synthesized from amorphous calcium phosphate. J. Am. Ceram. Soc. 107, 2809–2822. https://doi.org/10.1111/jace.19631.

Peng, S.-Y., Lin, Y.-W., Lee, W.-H., Lin, Y.-Y., Hung, M.-J., Lin, K.-L., 2023. Removal of Cu2+ from wastewater using eco-hydroxyapatite synthesized from marble sludge. Mater. Chem. Phys. 293, 126854. https://doi.org/10.1016/j.matchemphys.2022.126854.

P. Ptáček Apatites and their Synthetic Analogues - Synthesis 2016 InTech Structure, Properties and Applications 10.5772/59882.

Raynaud, S., Champion, E., Bernache-Assollant, D., Thomas, P., 2002. Calcium phosphate apatites with variable Ca/P atomic ratio I. Synthesis, characterisation and thermal stability of powders. Biomaterials 23, 1065–1072. https://doi.org/10.1016/S0142-9612(01)00218-6.

Romero, M., Padilla, I., Contreras, M., López-Delgado, A., 2021. Mullite-based ceramics from mining waste: a review. Minerals 11, 332. https://doi.org/10.3390/min11030332.

Royal Decree 646/2020, of July 7, which regulates the disposal of waste by depositing it in a landfill., n.d.

Sadli, N., May, A., Hamidouche, M., Henniche, A., Belhouchet, H., Boudouh, H., 2024. Investigations on kaolin mixtures: Impact on mullite formation kinetics and microstructure evolution. Int. J. Appl. Ceram. Technol. 21, 3950–3966. https://doi.org/10.1111/ijac.14820.

Segundo, I.D.B., Gomes, A.I., Souza-Chaves, B.M., Park, M., dos Santos, A.B., Boaventura, R.A.R., Moreira, F.C., Silva, T.F.C.V., Vilar, V.J.P., 2021. Incorporation of ozone-driven processes in a treatment line for a leachate from a hazardous industrial waste landfill: Impact on the bio-refractory character and dissolved organic matter distribution. J. Environ. Chem. Eng. 9, 105554. https://doi.org/10.1016/j.jece.2021.105554.

Singh, D., Friis, H.A., Jettestuen, E., Helland, J.O., 2022. A level set approach to Ostwald ripening of trapped gas bubbles in porous media. Transp. Porous Media 145, 441–474. https://doi.org/10.1007/s11242-022-01859-4.

Sokolar, R., Nguyen, M., 2024. Anorthite ceramics: grog and clay selection for lowering the sintering temperature. J. Asian Ceram. Soc. 12, 129–140. https://doi.org/10.1080/21870764.2024.2320448.

Soto-Cruz, F.J., Pérez-Moreno, S.M., Barba-Lobo, A., Bolívar, J.P., Casas-Ruiz, M., García, V.M., Gázquez, M.J., 2025. Acid neutralisation capacity (ANC) of biomass ashes and its potential use for phosphogypsum leachate cleaning. J. Water Process Eng. 70, 106968. https://doi.org/10.1016/j.jwpe.2025.106968.

Soto-Cruz, F.J., Pérez-Moreno, S.M., Ceccotti, E., Barba-Lobo, A., Bolívar, J.P., Casas-Ruiz, M., Gázquez, M.J., 2024. Valorisation diagnosis of waste from the decontamination of phosphogypsum leachates through a combined calcium carbonate/hydroxide process. Heliyon 10, e30610. https://doi.org/10.1016/J.HELIYON.2024.E30610.

Soto-Cruz, F.J., Rosales, J., Bolívar, J.P., Ramos-Lerate, I., Agrela, F., Gázquez, M.J., 2025. Phosphogypsum leachate cleaning waste as partial cement replacement in mortars. Results Eng. 28, 107913. https://doi.org/10.1016/j.rineng.2025.107913.

Takei, T., Imazawa, N., Miura, A., Kumada, N., Ogihara, K., 2013. Conversion of calcium sulfite waste to hydroxyapatite. Powder Technol. 237, 400–405. https://doi.org/10.1016/j.powtec.2012.12.022.

Tayibi, H., Choura, M., López, F.A., Alguacil, F.J., López-Delgado, A., 2009. Environmental impact and management of phosphogypsum. J. Environ. Manage. 90, 2377–2386. https://doi.org/10.1016/j.jenvman.2009.03.007.

Unscear, 1993. Report. sources, effects and risks of ionizing radiation. UN Publications. ISBN, 92-1-142200-0.

Uskoković, V., Marković, S., Veselinović, L., Škapin, S., Ignjatović, N., Uskoković, D.P., 2018. Insights into the kinetics of thermally induced crystallization of amorphous calcium phosphate. Physical Chemistry Chemicla Physis 20, 29221–29235. https://doi.org/10.1039/C8CP06460A.

Vasić, M.V., Kuzmanović, P., Hansman, J., Knežević Radić, J., Muñoz Velasco, P., Awoyera, P.O., 2025. Chemical, technological, and radiological characteristics of raw clay and shale mixtures for ceramic brick production. J. Radioanal. Nucl. Chem. 334, 4859–4874. https://doi.org/10.1007/s10967-025-10229-5.

Wu, F., 2024. The treatment of phosphogypsum leachate is more urgent than phosphogypsum. Environ. Res. 262, 119849. https://doi.org/10.1016/J.ENVRES.2024.119849.

Wu, S.-C., Hsu, H.-C., Wang, H.-F., Liou, S.-P., Ho, W.-F., 2023. Synthesis and Characterization of Nano-Hydroxyapatite Obtained from Eggshell via the Hydrothermal Process and the Precipitation Method. Molecules 28, 4926. https://doi.org/10.3390/molecules28134926.

Yan, M., Wang, H., Wei, R., Li, W., 2024. Arsenic trioxide: applications, mechanisms of action, toxicity and rescue strategies to date. Arch. Pharm. Res. 47, 249–271. https://doi.org/10.1007/s12272-023-01481-y.

Yuan, Z., Cai, G., Gao, L., Wu, M., Kong, L., Bai, J., Bai, Z., Li, H., Li, W., 2023. The physical encapsulation and chemical fixation of Zn during thermal treatment process of municipal solid waste incineration (MSWI) fly ash. Waste Manag. 166, 203–210. https://doi.org/10.1016/j.wasman.2023.05.007.

Zanelli, C., Conte, S., Molinari, C., Soldati, R., Dondi, M., 2021. Waste recycling in ceramic tiles: a technological outlook. Resour. Conserv. Recycl. 168, 105289. https://doi.org/10.1016/j.resconrec.2020.105289.

Zhang, Y., Tao, M., Shen, D., Zheng, S., He, Y., Ying, G., Ying, J., Shi, Y., 2015. Toxicity leaching of brick making from sludge containing heavy metals. Chinese Journal of Environmental Engineering 9, 1984–1988.

Zheng, Y., Baudet, B.A., Delage, P., Pereira, J.-M., Sammonds, P., Singh, P., Singh, D.N., 2025. Pore changes in an illitic clay during one-dimensional compression. Géotechnique 75, 1093–1096. https://doi.org/10.1680/jgeot.24.00991.